

26 Abstract

27 The Dominga district, northern Chile, shows a spatial and genetic affinity among distinctive
28 structural elements and occurrence of Fe-Cu-rich paragenetic mineral assemblages. Deep seated, NE-to-
29 EW striking structural elements form a right-lateral duplex-like structural system (Early Structural
30 System, ESS) that cut regionally altered (stage I) rocks. The system served as a locus and as path for the
31 emplacement of a Biotite-Magnetite alteration/mineralization (stage IIa) as veins and Fe-bearing layers
32 following altered volcano-sedimentary strata. NW-striking Actinolite-Magnetite hydrothermal breccias,
33 coeval with and part of the ESS, include Apatite (stage IIb) crystallized at ca. 127.0 ± 15.0 Ma (U-Pb). The
34 ESS was also the loci of a alteration/mineralization represented by K-Feldspar and Albite (stage IIIa) and
35 Fe-Cu-rich (Vermiculite-Anhydrite-Chalcopyrite, stage IIIb) mineral associations. Shallowly developed,
36 NNE-striking, left-lateral structural elements defining El Tofo Structural System (ETSS) – probably part
37 of the Atacama Fault System – clearly crosscut the ESS. Minerals associated with
38 alteration/mineralization stage IIIb also occurs as veins and as part of hydrothermal breccias of the ETSS,
39 marking the transition from the ESS to ETSS. Molybdenite crystals associated to alteration/mineralization
40 stage IIIb indicate an age of 127.0 ± 0.65 Ma (Re-Os). Both the ESS and ETSS were cut by left-lateral,
41 NW- to EW-striking shallowly developed structural elements (Intermediate Structural System, ISS) on
42 where a Hematite-Calcite-rich paragenetic assemblage (stage IV) occurs mostly as infill material of veins
43 and fault-veins. The ISS is, in turn, cut by NS-striking, left-lateral, shallowly developed structural
44 elements (Late Structural System, LSS) with no evidence of alteration/mineralization. Estimated strain
45 and stress fields indicate an overall NW-trending shortening/compression and NE-trending
46 stretching/tension strike-slip regime, probably due to left-oblique subduction during the Mesozoic.
47 However, the orientations of the stress and strain fields calculated for each structural system suggest a
48 back-and-forth rotation/shift pattern – as fields change between transtensional and tranpressional – as
49 transition between structural systems and between alteration/mineralization stages.

50

51 Keywords: Fe-rich deposit, Structural elements and systems, Stress and Strain, Mineral
52 Paragenesis, Isotopic dating.

53

54

55 1. Introduction

56

57 The Dominga deposit, located ca. 60 km north of La Serena (Fig. 1), corresponds to an Fe-Cu-rich
58 ore deposit emplaced into volcano-sedimentary rocks correlated to the Punta del Cobre Formation (e.g.
59 Creixell y Arévalo, 2009) and into previously uncharted subvolcanic bodies of dioritic composition
60 including andesitic and dioritic porphyries and microdiorites, altogether referred as the Porphyric Dioritic
61 Complex. Perhaps due to its geographic location and mineralogical similarities with other Fe-rich
62 deposits in the region, Dominga may be included within the so-called NS-striking “Cretaceous Iron Belt”
63 (e.g. Geijer, 1931; Ruiz et al., 1965; Park, 1972; Espinoza, 1984, 1990; Oyarzún and Frutos, 1975, 1984;
64 Menard, 1986; Ruiz and Peebles, 1988) extending from the localities of Taltal to La Serena and
65 subparallel to the actual Coastal Cordillera in Northern Chile (Fig. 1). The belt includes several world-
66 class IOCG (Fe-Cu-Au-Ag-U-Co-REE) deposits of Mesozoic age (e.g. Marschik et al., 1997; Marschik
67 and Fontboté, 2001; Mathur et al., 2002; Arévalo et al., 2006; Gelcich et al., 2005; Arévalo et al. 2009;),
68 on where mineralization occurs as veins, hydrothermal breccias and/or stratiform bodies, or, simply, as
69 irregular-shaped bodies (e.g. Vivallo et al., 2008; Vivallo, 2009).

70 Several deposits within the belt are spatially and/or temporally associated with left-lateral NNE- to
71 N-striking and NNW- to WNW-striking structural elements (e.g. Candelaria, Carola, Manto Verde and
72 Teresa de Colmo deposits). Due to similarities in kinematics and orientation of associated structural
73 elements, plus available geochronological data, the genesis of these deposits has been either assigned or
74 correlated to the Atacama Fault System (AFS) (e.g. Vila et al., 1996; Sillitoe, 2003). Consistently, several
75 models that link the activity of the AFS and different alteration/mineralization stages in Fe-rich deposits
76 in northern Chile have been proposed (e.g. Arévalo et al. 2009; Marschik et al., 1997; Marschik and
77 Fontboté, 2001; Mathur et al., 2002; Gelcich et al., 2005; Arévalo et al., 2006). However, certain deposits
78 spatially within the “Cretaceous Iron Belt” are instead related to right-lateral NE- to ENE-striking
79 structural elements apparently unrelated and previous to the activity of the AFS (e.g. Cembrano et al.,
80 2009); as for example the deposits of Cerro Negro, El Salado (Gelcich et al., 1998), Carrizal Alto (Ruiz et
81 al., 1965) and Mantos de Punitaqui (Ruiz et al., 1965) (Fig. 1). Some other deposits seem to be partly
82 related to such NE- to ENE-striking structural elements; for example, at Candelaria, Bonson et al. (1998)
83 describes a set of NE-striking right-lateral structural elements that host part of the mineralization, but
84 assigned them to the, left-lateral, AFS.

85 Available geochronological data for some Fe-rich deposits spatially within the metallogenic belt
86 argue for a main mineralization stage in the range of ca. 125-100 Ma, somehow synchronous with the
87 left-lateral activity of the AFS (Arévalo et al., 1999; Marschik et al., 1997; Vila, 1996; Marschik and
88 Fontboté, 2001; Ulrich and Clark, 1999; Scheuber and González, 1999; Mathur et al., 2002; Grocott and
89 Taylor, 2002; Vivallo et al., 2008; Creixell et al., 2009; Creixell and Arévalo, 2009; and references
90 therein). However, Fe-rich deposits associated with right-lateral structural elements seem to be somehow
91 older (>125-140Ma; e.g. Gelcich et al., 2005), thus arguing for a possible earlier, unrelated to the AFS,
92 mineralization stage.

93 This opens the possibility that alteration/mineralization associated with right-lateral NE-striking
94 structural elements may have been overseen or wrongly assigned to the AFS on some of the Fe-rich
95 deposits in northern Chile. If so, implies that (at least part of) the Fe-rich mineralization could be
96 unrelated to – and older than – the activity of the AFS (e.g. Grocott and Taylor, 2002; Cembrano et al.,
97 2009). It also implies that the traditional view of one NS-striking metallogenic belt may be biased, a
98 misleading concept that hinders the understanding of Fe-ore formation and of mineral exploration in
99 northern Chile. Then the question arises to whether the Dominga ore deposit was the result of a pre-, syn-
100 or post-AFS mineralization stage? in particular, are the structural elements at Dominga associated with
101 the AFS? or, instead, with another independent structural system?

102 At the Dominga district, Fe-rich mineralization occurs as veins, hydrothermal breccias and strata-
103 like bodies, spatially and geometrically associated with particular structural elements having defined
104 morphologies and preferential displacement and striking directions. These structural elements are: (1)
105 NE- to EW-striking, right-lateral, foliated ultracataclasites and cataclasites, which seem to form a
106 kilometer-size duplex geometry; (2) NNW- to EW-striking breccias bodies and other shear zones with
107 left-lateral displacement sense; (3) NS- to NE-striking, left-lateral cataclasites, fault-breccias, slip-
108 surfaces and fault-veins; and (4) NW- and NE-striking hydrothermal breccias. Besides differences in
109 orientation and kinematics, structural elements show marked differences in morphology, style of
110 deformation, average width and associated mineral assemblages (Fig. 2, 3). Then, we ask, which set or
111 sets of structural elements host the main Fe-ore mineralization? Did these structural elements provide the
112 necessary conditions for fluid migration and/or later emplacement? Did any or some of these sets of
113 structural elements only modify the geometry of the ore deposit?

114 In this work, we present newly collected, processed and integrated structural, mineral paragenesis
115 and isotopic data used to construct a conceptual model that accounts for the tectono-metallogenic
116 evolution of the Dominga Fe-rich deposit. The model focuses on the spatial and temporal relations among
117 and between structural elements, structural systems and alteration/mineralization stages. Heterogeneous,
118 polyphasic, fault-slip data was analyzed to estimate the orientation and characteristics of the strain and
119 stress fields that drove the tectonic evolution of the district. Paragenetic and isotopic data provide relative
120 and absolute chronology constraints between and among alteration and mineralization mineral phases and
121 alteration/mineralization stages.

122 123 2. Methodology 124

125 Within the Dominga district we measured a total of 962 structural elements including foliated
126 ultracataclasites and cataclasites, non-foliated cataclasites, fault- and hydrothermal breccias, gouge bands,
127 slip-surfaces, fault-veins and veins filled with different mineral assemblages (Fig. 2, 3). Also included,
128 yet less exposed, are mylonites and veins showing evidence of polyphase deformation. Data logged from
129 each structural element includes: (1) thickness, (2) orientation, (3) orientation of the slickenline (or any
130 other kinematic indicator; e.g., Petit, 1987; Doblas, 1998), (4) the sense of displacement (e.g. Angelier,
131 1994; Petit, 1987), and (5) associated mineral occurrences. Among gathered data, only slip-surfaces and
132 fault-veins (n=261) have complete fault-slip datum suitable for further strain and stress analyses (Fig. 2c).

133 We also recorded the orientation of foliation (S) and shear (C) planes from S-C textures
134 macroscopically observed on foliated ultracataclasites and cataclasites (Fig. 2d) and used them to
135 calculate the orientation of the slip direction on the C-plane. This corresponds to the vector on the C plane
136 normal to the intersection of C and S planes. The sense of displacement was taken from the angular
137 relationship between the same C and S planes. We considered this as a second set of fault-slip data
138 (hereafter referred as S-C derived fault-slip data) suitable for estimation of both strain and stress fields.

139 Mineral occurrence – spatially and/or locally associated with an structural element – its relative
140 concentration, grain-size, crosscutting relationships, crystal morphology, as well as the relative
141 orientation and location with respect to nearby structural elements were logged on and locally around
142 each structural element. We also examined under optical microscope a total of 58 thin sections (20 of
143 them oriented), collected both from surface and from drill cores, to aid identification and definition of

144 mineral paragenetic assemblages, their relative temporal relationships, grain-size and morphology, and
145 spatial and/or temporal relations with related structural elements.

146 Strain analysis, carried with the aid of the FaultKin software (v7.0, freely available at
147 <http://www.geo.cornell.edu/geology/faculty/RWA/programs/faultkin.html>), transforms the fault-slip
148 datum into a pair of axes representing the maximum (shortening, P) and minimum (stretching, T) strain
149 axes (e.g. Marrett and Allmendinger, 1990). Hence, the method only transforms the fault-slip datum into
150 a pair of orthogonal and kinematically related axes whose orientation depends on that of the structural
151 element and of the kinematic indicator. The averaged orientations of P and T axes could then provide the
152 overall shortening and stretching orientations at the study area or at a regional scale.

153 Stress analyses were conducted using the Multiple Inverse Method (MIM v4.17/6.02; Yamaji,
154 2000; <http://www.kueps.kyoto-u.ac.jp/~web-bs/tsg/software/mim/>). The method has been developed to
155 separate homogeneous stress fields recorded on an heterogeneous fault-slip data set resulted from
156 polyphase deformation, being successfully used to estimate and separate homogeneous stress fields from
157 both natural and simulated heterogeneous fault-slip data sets (e.g. Sippel et al., 2009; Veloso et al., 2009;
158 Federico et al., 2010; and references therein). The method estimates a common best-fit stress field – based
159 on the Wallace-Bott hypothesis (Wallace, 1951; Bott; 1954) – associated with a sub-group of “k”-number
160 fault-slip data extracted from the entire data set. The orientations of the calculated principal axes are then
161 plotted on a couple of stereograms – one for σ_1 and other for σ_3 axes solutions (Yamaji, 2000). Each
162 plotted axis symbol includes a tail that points towards the complementary axis (i.e. tail on σ_1 points
163 towards σ_3), color-coded according to its stress ratio ($\phi = (\sigma_2 - \sigma_3) / (\sigma_1 - \sigma_3)$). The orientation of the best-fit
164 stress field is then, iteratively, calculated for all possible sub-groups extracted from the entire fault-slip
165 data set. Common and compatible stress field solutions are seen as clusters of principal axes with similar
166 colors and with tails pointing towards a common orientation (e.g. Yamaji, 2000; Otsubo and Yamaji,
167 2006).

168 In order to estimate mineralization ages we analyzed two samples, one by means of Re-Os isotopic
169 dating (in molybdenite) at the Sulfide and Source Rock Geochronology and Geochemistry Laboratory at
170 Durham University, UK, and other by U-Pb isotopic dating (in apatite) at the University College of
171 London Labs, UK. Methodology details for Re-Os dating can be obtained from Selby and Creaser (2001).
172 In brief, molybdenite is digested in carius tube with a known amount of Re and Os tracer solution with

173 *aqua-regia*. Osmium is isolated and purified via solvent extraction and micro-distillation. Re is isolated
174 and purified by solvent extraction and anion chromatography. Both Re and Os isotope compositions were
175 determined using Faraday cups on a Thermo Scientific TRITON mass spectrometer.

176 U-Pb dating was carried out by LA-ICP-MS, using a New Wave NWR 193 excimer laser with a
177 standard volume cell connected to an Agilent 7700x quadrupole mass spectrometer. Fourteen
178 35µm diameter spots were ablated for 30 seconds at 10Hz and 2.5 mJ/cm² fluence, preceded by 15
179 seconds of warmup time during which blanks were collected. Madagascar (MAD) apatite was used as a
180 U/Pb age standard (486.85 ± 0.85 Ma, Thomson et al., 2012) and NIST SRM612 as a concentration
181 standard (Pearce et al., 1997). Sample-standard bracketing was performed using Glitter 4.4.3 (Griffin et
182 al., 2008).

183 Textural and semi-quantitative chemical data were obtained through scanning electron microscopy
184 (SEM) in a FEI Quanta 250 SEM equipped with energy-dispersive X-ray spectrometry (EDS) detector at
185 the Department of Geology of the Universidad de Chile.

186

187 3. Structural Elements

188

189 To keep identification and classification of geological structures as simple and descriptive as
190 possible, devoid of any *a priori* interpretation, we define a structural element as a physical planar/tabular
191 object that may contain an infill material such as hydrothermal crystallized, magmatic, cataclastic,
192 brecciated (sheared and broken), crystal-plastically or plastically deformed materials. Therefore, a
193 structural element is at the outcrop scale defined by its nature and appearance, with no assumptions or
194 interpretations involved.

195 Mylonites are scarce at Dominga (Fig. 2) but when present they strike ENE, ca. N60°-70°E, yet
196 few show NW-strikes; all with thicknesses of tens of centimeters (Fig. 3). Kinematic indicators show
197 consistent right-lateral displacements for the NE-striking mylonites, and left-lateral for the NW-striking
198 ones.

199 Foliated ultracataclasites are the most common type of structural element at Dominga, displaying a
200 rather constant preferential ca. N60°E-striking direction (Fig. 2). Thickness varies between few cm's up to
201 several tens of meters (maximum ca. 50m) (Fig. 3), yet in average they are about 10-20 cm thick.
202 Kinematic indicators are consistent among these structural elements indicating right-lateral displacement.

203 Similarly, and as common as foliated ultracataclasites, foliated and non-foliated cataclasites
204 display a NE-striking preferential orientation, yet some have N- to NNE-strikes (Fig. 2d). Thickness
205 varies between few tens of centimeters up to ca. five meters, but in average foliated cataclasites are ca. 50
206 cm thick whereas non-foliated cataclasites are ca. 5-10 cm thick, slightly thicker and thinner, respectively,
207 when compared with foliated ultracataclasites. Kinematic indicators are consistent and evidence right-
208 lateral displacements for NE- to ENE-striking cataclasites and left-lateral displacements for those with N-
209 to NNE-strikes.

210 Ultracataclasites and (foliated and non-foliated) cataclasites cut and displace the volcano-clastic
211 rocks of the Punta del Cobre Formation, thus suggesting that these are, at least, younger than 140 Ma (e.g.
212 Creixell and Arévalo, 2009). Included into foliated cataclasites, we found large (ca. 5-10 cm diameter)
213 porfiroclasts of hydrothermal breccia (with a Mag-Act-rich matrix; mineral abbreviations after Whitney
214 and Evans (2010). As shown further, hydrothermal breccia bodies also include relicts of foliated
215 (ultra)cataclasites, similar in texture and morphology to those with preferential NE-strikes and right-
216 lateral displacements. This suggests a coeval activity/development of the hydrothermal breccia bodies and
217 ultracataclasites and (foliated and non-foliated) cataclasites with right-lateral displacements.

218 Fault-breccias display widely spread strikes with a slight preference for NE-, NNW- to NNE- and
219 EW-strikes (Fig. 2). Thickness varies between tens of centimeters to ca. one meter (Fig. 3), being in
220 average about 20-30 cm thick, similar to non-foliated cataclasites. No kinematic information could be
221 obtained from these structural elements. Gouge bands, less common in the Dominga district, exhibit
222 thicknesses ranging from few millimeters up to few centimeters (Fig. 3). Similar to fault-breccias,
223 kinematic information from gouge bands could not be obtained with any reasonable certainty.

224 By definition in this work, slip-surfaces have no thickness, being essentially just striated surfaces.
225 At Dominga, these structural elements display widespread striking directions, showing slightly
226 preferential orientations with NW- and EW-strikes and, in a lesser amount, NNE- to ENE-strikes (Fig. 2,
227 3). Kinematic indicators (e.g. steps, R and R' fractures; e.g. Doblas, 1998; Petit, 1987) indicate left-lateral
228 (with minor dip-slip, normal) displacements for NW- and for some EW-striking slip-surfaces, and right-
229 lateral displacements for NNE- to ENE- and (some) EW-striking slip-surfaces.

230 Fault-veins, despite of their mineral infill, have thicknesses ranging from few millimeters up to
231 centimeters (Fig. 3). These structural elements display clear preferential strike directions: NW, ENE and

232 NNE (Fig. 2, 3). Observed slickenfibers, steps and striated minerals indicate consistent left-lateral
233 displacement with minor amounts of dip-slip (commonly normal) displacement of NE blocks.

234 Veins filled with different minerals (and combinations of them) outcrop all over the Dominga
235 district (Fig. 2). Most common mineral fillings include, (either alone or associated) Mag, Ap, Qtz, Hem
236 (specular), Act, Cal, Ep and, locally, Kfs. We also observed patches of Cu-oxides spatially associated
237 with some minerals infills, especially those of Cal. Vein mineral filling associated with specific
238 paragenetic associations (see further) show clear preferential strikes; for example: (1) veins with Ap or
239 Ap+Act are common in the strike range of N30°-70°E, whereas those with Ap+Mag tend to be more
240 common in the strike range between N30°-50°W; (2) veins with Hem (specular), alone or with other
241 minerals, have strikes between ca. N10°-50°W.

242 Hydrothermal breccias mostly outcrop in the easternmost part of the Dominga district. Individual
243 bodies have tabular shapes, commonly arranged on an *en echelon* geometry (Fig 4), that can be followed
244 tens of meters. Two distinct sets of hydrothermal breccia bodies were observed; the first in the south-
245 easternmost part of Dominga (hereafter referred to as “Dominga Breccia”) as a series of *en echelon*,
246 subvertical bodies including massively altered clasts (Mag-Act-Ap; ca. 30-50%) immersed in a fine-
247 grained matrix of Mag-Act (and Ap in places). Observed thicknesses are rather constant, being about 8-10
248 m. These structural elements emplaced onto altered (Fe-rich) volcano-clastic strata of the Punta del Cobre
249 Formation, suggesting that are younger than ca. 140 Ma, as well as than the alteration/mineralization
250 observed in the rocks of the Punta del Cobre Formation and of the Porphyric Dioritic Complex. The
251 second set of hydrothermal breccia – outcropping in the north-easternmost part of Dominga – is a
252 massive, irregular, and diffuse series of *en echelon*, NE-striking bodies including abundant clasts of the
253 surrounding host rock (andesite) immersed into a matrix of massive Ap crystals. Among these elements,
254 we found a NE-striking, tabular-shaped hydrothermal breccia subparallel to those with Ap-rich matrix,
255 similar in texture, appearance and overall composition to the “Dominga Breccia”.

256 Mapped and measured structural elements, regardless of its type (ultracataclasite, slip-surface,
257 vein, etc.), can be arranged into 5 populations based on their preferential orientations. These populations
258 of structural elements - with subvertical dips and labeled A to E on figure 2a, b – have strikes in the
259 following ranges: (A) N50°-70°E, (B) N30°-60°W, (C) N80°-100°E, (D) N20°-40°E, and (E) N°0-10°E.

260 Population A (Fig. 2) – ca. N50°-70°E – includes mostly ultracataclasites and (foliated and non-
261 foliated) cataclasites showing right-lateral kinematic indicators and, to a lesser amount, by slip-surfaces

262 and fault-veins also evidencing right-lateral displacements. Structural elements from this population are
263 cut and left-laterally displaced by structural elements (commonly fault-veins and slip-surfaces) with
264 strikes between N30°-60°W (population B; Fig. 2), suggesting that these two sets of structural elements
265 were non-coeval.

266 Fe-mineralization, spatially related to the structural elements of population A, occurs as veins,
267 massive patches and mineral clusters located either within or few meters away (<5m) from the structural
268 elements. Also, Fe-mineralization occurs as strata-like bodies, roughly following the strata of the Punta
269 del Cobre Formation. Thin-sections evidence that foliated ultracataclasites and (foliated and non-foliated)
270 cataclasites contain two different types of Mag crystals with different textures, together with Act and Bt
271 crystals which also display differences in grain-size and shape.

272 Population B (ca. N30°-60°W) includes mostly slip-surfaces and fault-veins evidencing left-lateral
273 displacements (Fig. 2a, b, 3). Ultracataclasites and (foliated and non-foliated) cataclasites are uncommon
274 in this orientation, but when present they show left-lateral displacements (Fig. 2f). Structural elements
275 from this population are cut, but apparently not significantly displaced, by fault-breccias, slip-surfaces
276 and fault-veins, all with strikes between N0°-10°E (Fig. 4). We observed slip-surfaces and fault-veins
277 with strikes between N30°-60°W cutting a series of tabular *en echelon* hydrothermal bodies (Mag-Act
278 matrix) of the “Dominga Breccia”.

279 Hem and Cal minerals (rarely together) are spatially and geometrically related to the structural
280 elements of population B. In places, Cal-rich veins show evidences of polyphase deformation (e.g.
281 hydrothermal or fault-breccia imposed over a former vein). Included in Cal-rich veins, we found oxidized
282 crystals of Ccp as well as boxwork of Py/Ccp.

283 Population C (ca. N80°-100°E) includes foliated ultracataclasites and cataclasites showing right-
284 lateral displacements (S-C texture), as well as slip-surfaces and fault-veins with left-lateral kinematic
285 indicators. Commonly, foliated ultracataclasites and cataclasites included in this population splay off
286 similar structural elements with strikes between N50°-70°E (population A), forming a kilometer-size
287 right-lateral duplex geometry (Fig. 4). Similarly, slip-surfaces and fault-veins included into population C
288 splay off similar structural elements with strikes between N30°-60°W (i.e. population B). This later spatial
289 arrangement is, however, fairly discontinuous – especially in the N80°-100°E strike direction – forming a
290 set of subsidiary structural elements rather than a duplex geometry.

291 Right-lateral foliated ultracataclasites and cataclasites are cut and left-laterally displaced by fault-
292 breccias and slip-surfaces with strike directions between N30°-60°W, but rarely by structural elements
293 with strikes in the range N0°-10°E (Fig. 4). Similarly, slip-surfaces and fault-veins included into
294 population C cut and displace structural elements with strikes between N50°-70°E (population A), as well
295 as ultracataclasites and (foliated and non-foliated) cataclasites with strikes ranging between N80°-100°E
296 (population C). Thus argues for the existence of two different and independent sets of structural elements
297 having N80°-100°E strikes; one associated to population A and other to population B (Fig. 2a, b). Fe-
298 bearing minerals associated with left-lateral structural elements of population C are the same as for
299 structural elements of population B (i.e. Hem and Cal, and locally oxidized Ccp), whereas minerals
300 associated with right-lateral structural elements of population C are the same as those of population A
301 (i.e. Mag-Act-rich).

302 Structural elements defining population D (ca. N20°-40°E) are common in the western part of
303 Dominga, mostly outcropping nearby to an abandoned Au-Cu mine (Fig. 4). This population includes
304 mostly foliated ultracataclasites and cataclasites, fault-breccias and slip-surfaces, which are contiguous
305 and continuous, forming a ca. 30 meter wide composite structural element (hereafter referred as “El Tofó
306 Deformation Band”) that evidences polyphase deformation. S-C textures of foliated ultracataclasites and
307 cataclasites within the deformation band evidence left-lateral displacement (Fig. 3c). Fault-breccias
308 commonly contain large clasts and vein relicts with massive Mag-Act-Ap(?) crystals immersed in a
309 cataclastic matrix (similar in texture to structural elements from population A) as well as relicts of Kfs-
310 filled veins. Slip-surfaces and fault-veins are rarely present within the band, yet they are common few
311 tens of meters eastward, forming an almost continuous, ca. 10m wide, band which probably represents a
312 fault-related damage zone.

313 Population E consists almost solely of slip-surfaces and fault-breccias (Fig. 2) observed mostly,
314 but not only, in the northern part of Dominga. Kinematic indicators on slip-surfaces (with strikes between
315 N0°-10°E) evidence left-lateral displacements. Fault-breccias commonly include relicts of crystals or
316 veins fill with Mag-Hem, Cal or Hem.

317

318 4. Structural Systems

319

320 Structural systems refer to a series of kinematically, temporally and genetically related structural
321 elements. Thus, different types of structural elements – such as ultracataclasites, cataclasites, fault-
322 breccias, slip-surfaces, etc. – may be part of the same system. Differences in morphology and deformation
323 style result from their development at different structural levels and/or under different strain/stress fields
324 during its history (e.g. Sibson, 1987; Scholz, 2002; Passchier and Trouw, 2005).

325 When considering cross-cutting relationships between and among different structural elements and
326 populations at Dominga it is possible to define four independent structural systems. Right-lateral
327 structural elements from population A and right-lateral foliated ultracataclasites and cataclasites and fault-
328 breccias from population C, define the oldest structural system (hereafter referred to as the Early
329 Structural System, ESS) with an internally consistent right-lateral duplex geometry (Fig. 4). Field
330 observations argue for a (pene)contemporaneous activity/development of these structural elements and
331 the *en echelon* tabular-shaped hydrothermal breccias. Moreover, the geometric arrangement between
332 these structural elements suggests that hydrothermal breccias with Mag-Act-rich matrix may have
333 developed in a tensional orientation (“T” subsidiary structure). The ESS also includes several types of
334 veins, mostly filled with Ap, Act, Mag, Mag+Qtz and Ep+Kfs (Fig. 2).

335 The structural elements of population D define a ca. N20°-40°E striking, left-lateral structural
336 element – hereafter termed El Tofo Structural System, ETSS – which seems to have concentrated most of
337 the deformation without the development of other similar nearby structural elements. Structural elements
338 from the ETSS cut and displaced those of the ESS (Fig. 4), yet they are cut and displaced by structural
339 elements of population B and, locally, by those of population E. Only veins with Qtz+Ep fillings could be
340 directly related to ETSS. Veins with Mag+Qtz, Mag, Ap and Ap+Act fillings (Fig. 2e) are often cut and
341 displaced by, or included as relicts on, the structural elements of ETSS, whereas those filled with Ep+Kfs
342 are both included as relicts and developed subparallel and within some of the structural elements of the
343 ETSS.

344 Slip-surfaces and fault-veins of population B and ca. 25% of fault-veins and slip-surfaces of
345 populations A and C, all evidencing left-lateral displacements, are geometrically related resembling a
346 discontinuous duplex geometry. These structural elements commonly cut and displaced structural
347 elements of the EES and the ETSS. So, similarities in morphology and kinematics plus observed
348 crosscutting relationships suggest that (the scarce) left-lateral structural elements of population A may
349 correspond to secondary structures of structural elements of population B, splaying off from these.

350 Consequently, it is possible to define an “Intermediate Structural System” (ISS) which includes the
351 structural elements of population B and the left-lateral structural elements of populations A and C (mostly
352 slip-surfaces, fault-veins and fault-breccias). Veins included in this system display Qtz, Qtz+Cal, Hem
353 (specular), Cal and locally Mag and Ep (Fig. 2) as mineral infills.

354 Structural elements from population E mostly outcrop in the northern part of Dominga, being
355 almost exclusively slip-surfaces and fault-breccias (Fig. 2). Observed crosscutting relationships indicate
356 that N0°-10°E striking structural elements cut (and displaced?) veins and fault-breccias from the ESS (Fig.
357 4) and fault-breccias and cataclasites of ETSS. Thus, we grouped the structural elements from population
358 E into, and defined, a “Late Structural System” (LSS). Veins filled with Ap or with Ep and/or Ep+Qtz are
359 commonly included as relicts within the fault-breccias of this system.

360

361 5. Strain and Stress Fields

362

363 The orientation of the strain field associated with a single structural element is uniquely defined by
364 its principal axes (P: shortening, T: stretching; e.g. Marrett and Allmendinger, 1990). However,
365 estimation of the best-fit strain field for a population of heterogeneous, polyphasic, fault-slip data requires
366 filtering, sometimes subjective, of the data. Prior knowledge about the relative temporality and/or
367 geometric relations among different structural elements may help on this (e.g. Sperner and Zweigel,
368 2010). Accordingly, we estimated the orientation of the strain field associated with the entire fault-slip
369 data, each of the identified structural systems and the S-C derived fault-slip data (Fig. 5).

370 Estimated orientations of P and T axes from the entire fault-slip data set yielded three
371 concentration maxima (Fig. 5a): P axes have NNW- to N- and WNW-trending azimuths with
372 subhorizontal plunges, and T axes have NE- to E- and nearly N-trending azimuths with subhorizontal
373 plunges. Namely, estimated strain fields correspond to strike-slip dominated deformation. However,
374 structural elements may behave differently depending on their orientation and the chosen maxima; for
375 example, NE-striking structural elements may behave as right- or left-lateral, depending on the maxima
376 considered.

377 Strain fields estimated for each structural system yielded, in general, similar orientations of their
378 principal axes (Fig. 5): P axes have NW- to NNW- and nearly E-trending azimuths, and T axes have NE-
379 to ENE- and nearly N-trending azimuths, both with subhorizontal plunges. When looking at individual

380 solutions, we observed that the orientations of P and T axes estimated for the EES are similar to those
381 estimated from the S-C-derived fault-slip data and roughly to one of the maxima obtained from the
382 analysis of the entire fault-slip data (Fig. 5). Similarly, P and T axes estimated for the other structural
383 systems have similar orientations when compared to the maximas obtained from the entire fault-slip data
384 (Fig. 5). Despite similarities, (relative) variations on the orientation of the principal strain axes from one
385 structural system to other are dissimilar, rotating/shifting both clock- (CW) and counterclock-wise
386 (CCW).

387 Estimation of the best-fit stress field using the MIM does not need any prior assumption over the
388 data as done previously. Clustering of principal stress axes defines a common best-fit stress tensor for a
389 (sub)population of the fault-slip data (e.g. Yamaji, 2000; Otsubo and Yamaji, 2006; Sippel et al., 2009;
390 Veloso et al., 2009; Federico et al., 2010). Henceforth, for the further analysis we used the entire fault-slip
391 data without any filtering criteria yet, given the source, we considered separately the S-C-derived fault-
392 slip data set.

393 Analysis of the entire fault-slip data yielded four different clusters of principal stress axes (labeled
394 A to D on Fig. 6a). Clusters A, B and C have subhorizontally oriented principal stress axes, with trends
395 ranging from ca. 100° to ca. 160° for the maximum (σ_1) and from ca. 20° to ca. 80° for the minimum (σ_3).
396 Cluster D has a moderately plunging σ_1 axis (azimuth ca. 70°) and a subhorizontal σ_3 and with ca. 340°
397 of azimuth. Thus, solutions A, B and C correspond to strike-slip regimes, whereas D is a mixture of
398 tensional and strike-slip regimes. Stress ratio values for each solution suggest that strike-slip regimes are
399 triaxial, varying between transpressional (TP), for solutions A and B, and transtensional (TT), for solution
400 C. Solution D represents a stress state close to uniaxial tension.

401 Estimated stress fields activate particular sets of structural elements (Fig. 6). Solution A activates
402 structural elements with strikes ranging from ca. N10°E to N60°W as left-lateral and those with strikes
403 between N70°-100°E as right-lateral. This suggests either a set of conjugate structural elements or a non-
404 coeval activity of both sets of structural elements resulted from, roughly, similarly oriented stress fields.
405 Solution B seems to activate structural elements with strikes slightly CW rotated/shifted with respect to
406 those activated by solution A. However, solution B also results in normal and reverse displacements of
407 some structural elements with strikes between ca. N30°-60°W.

408 Solution C activates structural elements with strikes between N10°-30°E as left-lateral and as right-
409 lateral those with strikes between N70°-90°W (Fig. 6). Solution D, on the contrary, activates structural
410 elements with strikes between ca. N30°-70°W as left-lateral and, to a lesser degree, those with strikes
411 between N70°-90°E and NW as left-lateral and as normal faulting, respectively.

412 Solutions E and F – obtained from the S-C-derived fault-slip data – have subhorizontal σ_1 axes
413 with WNW- and NW-trending azimuths, respectively. The σ_3 axes of solution E are well clustered on a
414 subhorizontal orientation, with a NE-trending azimuth; whereas solution F has rather a widespread
415 distribution of its σ_3 axes, yet these seem to cluster close to those of solution E but with steeper plunging
416 angles (Fig. 6). Namely, these solutions represent triaxial strike-slip and tensional/strike-slip regimes,
417 respectively. Structural elements activated either by solutions E or F are similar, i.e. structural elements
418 with NE- to ENE-strikes as right-lateral. Differences among structural elements activated by solution E
419 and F are given only by a couple of fault-slip data, which may respond as left-lateral instead of right-
420 lateral depending on which solution is considered.

421

422 6. Paragenetic Assemblages

423

424 We identified seven independent mineral associations based on contact and crosscutting
425 relationships. Main mineral alteration phases correspond to Bt, Act, Qtz, Ep, Ab, Kfs, Anh, Allantite
426 (Aln), Vermiculite (Vrm) and Cal; whereas mineralization mineral phases correspond to Ap, Mag, Hem
427 (specular), Py and Ccp (Fig. 7).

428 The earliest identified mineral association corresponds to a mixture of disseminated, pervasively
429 distributed, fine-grained Bt and Mag crystals spatially associated with Py and fine-grained Act, and
430 locally with Ttn crystals (Bt \geq Mag>Py>Act>Ttn association), all crystallized into the sedimentary rocks of
431 the Punta del Cobre Formation and of the Porphyric Dioritic Complex (Fig. 7b). Mag crystals exhibit
432 exolution textures suggesting cooling from high temperature (e.g. Butler, 1992; Tauxe, 1998).

433 Coarser Mag and Bt crystals display textures that coexist with Qtz, Act and Ttn, and locally, with
434 Py crystals (Mag+Bt+Qtz \pm Act \pm Ttn \gg Py association). This association occurs as disseminated or
435 cumulated blobs of crystals (Bt+Mag-rich), as the matrix of hydrothermal breccias, as constitutive
436 material of (ultra)cataclasites, as total or nearly complete replacement and obliteration of the host rock as

437 strata-like bodies, and as vein-filling material (as Bt+Qtz+Mag+Py or Qtz+Mag infills) (Fig. 7c, d). In the
438 groundmass of andesitic rocks, part of the Porphyry Dioritic Complex, coarse-grained Mag and Bt
439 crystals often grew onto similar fine-grained mineral phases. Mineralogically associated veins also cut
440 rocks having disseminated fine-grained Mag, Bt and Act.

441 Medium- to coarse-grained Act, Ap, Qtz together with medium-grained Py and Mag crystals
442 locally occurs as the matrix of hydrothermal breccias (Act+Mag+Py; Ap+Act+Mag+Py) and as filling
443 material of cm-wide veins (Act+Mag+Qtz; Ap). Commonly medium-grained Mag crystals, and in places
444 together with Py, are included in the cleavage planes of Act crystals (Fig. 7e). Field observations indicate
445 that hydrothermal breccias with Act+Mag+Ap-rich matrix cut veins filled with and rocks altered by
446 coarse the Mag+Bt+(Qtz±Act±Ttn)-rich association.

447 Veins filled with Kfs±Ep±Ab±Mag (from border to center), with Qtz+Kfs, with Qtz+Ab+Mag,
448 and with Qtz+Ep (association Qtz>>Ep=Ab>>Kfs>>Mag) commonly cut the rocks of the Punta del
449 Cobre Formation and of the Porphyric Dioritic Complex, as well as hydrothermal breccias with
450 Bt+Mag+Ap matrix. Qtz-Ep-Ab association also occurs as filling material of voids in some of the
451 volcanic rocks outcropping at the Dominga district. We also observed Kfs selectively replacing Pl crystals
452 in andesitic rocks of the Porphyric Dioritic Complex (Fig. 7f).

453 Hydrothermal breccias, displaying Anh>Aln>Ccp>Py≥Mag matrix and relicts clasts with coarse-
454 grained Bt+Mag crystals ((Anh>Aln)>Ccp>Py≥Mag association) commonly cut the massively Fe-altered
455 strata of the Punta del Cobre Formation. Coarse-grained Bt crystals exhibit reaction borders with Ahn
456 crystals which partially obliterate their host crystals; Aln and Ccp crystals exhibit intergrowth textures
457 (Fig. 7g, h). Also, small veins with Ccp+Py(+Ahn?) fillings cut coarse-grained Act and Ap crystals.

458 Veins with a Vrm+Qtz+Py≥Ccp association infill (Fig. 7i) also cut rocks and strata strongly
459 altered by a coarse-grained Bt+Mag-rich association. Also, medium- to coarse-grained size Mag crystals
460 are cut by Vrm ones. Unfortunately, no other crosscutting relationships were observed, yet spatial
461 relations among mineral phases and associations suggest that the Vrm+Qtz+Py≥Ccp paragenesis post-
462 dates or it is penecontemporaneous with the crystallization of Ep.

463 Hydrothermal-breccias and fault-veins exhibiting a Cal-rich matrix or slickenfibers commonly
464 include oxidized forms and relicts of Ccp within and between Cal crystals (Fig. 7j). These hydrothermal
465 breccias and fault-veins often cut Vrm-rich and coarse Bt+Mag-rich veins. Similarly, Qtz+Hem filled
466 veins (Fig. 7k) commonly cut massively Mag-rich altered strata, displaying both fine- and coarse-grained

467 Bt+Mag crystals together with coarse Act+Mag crystals. Though rare in the field, we observe some small
468 veins filled with Cal (center) and Hem (border).

469

470 7. Geochronological Isotopic Constraints

471

472 7.1. Re–Os dating

473 To provide the best age of mineralization Re–Os analysis was carried out on molybdenite (Table 1;
474 sample DS11-134A). Although molybdenite is scarce at Dominga, trace molybdenite is observed in an
475 Anh-matrix breccia from a drill core at 490 m depth (Fig. 8; sample DS11-134A). The breccia consists of
476 angular clasts of host rock (Bt-altered andesite) and aggregates of Act (1.5 mm)-Bt (1 mm) into an
477 hydrothermal matrix of coarser Ccp (up to 6 mm)-Py (8 mm) and finer Anh (1.5 mm)-All (1 mm)-Mag
478 (0.3 mm)-Qtz (1mm). In the matrix, very fine-grained molybdenite (50-150 μm) coexists with Ahn-All-
479 Py-Ccp-Qtz indicating that Mo and Cu mineralization occurred during the same paragenetic stage (IIIb)
480 (Fig. 8). Cutting relationships show that Anh-matrix breccia cuts main Mag-rich ore bodies. Pure
481 molybdenite (0.005 mg) was obtained from the sample by crushing, washing, drying, and handpicking
482 under a microscope. The molybdenite possesses ~886 ppm Re and ~1180 ppb ^{187}Os (Table 1). The ^{187}Re -
483 ^{187}Os age of the molybdenite is 127.0 ± 0.65 Ma, which is interpreted as the time of Fe-Cu mineralization
484 (stage IIIb).

485

486 7.2 U-Pb dating

487 We collected one sample containing apatite from a drill core at 170 m depth (sample DN11-136) for U-Pb
488 dating (Table 1; sample DS11-136). Ap crystals occur mainly as the matrix of hydrothermal breccias
489 accompanied by Mag and Act (Fig. 8). Three cm-sized fragments of apatite breccia were cut with a rock
490 saw and polished with 4000-grit grinding paper. About 20 grains/spots were analyzed by laser ablation.
491 Given the low (~1 ppm) U and Th concentrations and young age of the samples, common Pb is a real
492 concern. No ^{204}Pb was measured for two reasons. First, the presence of an isobaric interference from
493 ^{204}Hg would have compromised any ^{204}Pb correction. Second, even in the absence of ^{204}Hg , adequately
494 measuring ^{204}Pb would require most of the analytical time at the expense of the ^{206}Pb and ^{207}Pb precision.
495 Instead, the common Pb problem was addressed by plotting all the samples on a Wetherill concordia
496 diagram (e.g. Ludwig, 2003), which yields a statistically robust isochron with a lower intercept of 127 Ma

497 ± 15 Ma (95% confidence interval) and an upper intercept of meaningless age driven by the common Pb
498 composition. It is considered the best crystallization age (500° C) of the hydrothermal apatite (Fig. 8c).
499 Field observations suggest that Ap-rich matrix breccias are older than the Fe-Cu mineralization, which is
500 consistent when considering the large error obtained from this sample. Additionally, no meaningful
501 intercept at 3583 ± 110 Ma could be obtained.

502

503 8. Discussion

504

505 8.1. Structural Levels

506

507 Broadly speaking, each type of structural element outcropping at the Dominga district is related to
508 a particular structural system. For example, nearly all structural elements of the ESS are ultracataclasites
509 and cataclasites sharing a common preferential NE- to EW-striking orientation and right-lateral
510 displacement direction, whereas the LSS includes mostly slip-surfaces, fault-breccias and gouge bands
511 with a common N- to NNE-strike and with left-lateral displacements (Fig. 2). Thus, the variety of
512 structural elements included in a particular structural system is a proxy to estimate the structural level on
513 where they developed. In general, such depth depends on several factors (e.g. temperature, pressure, rock
514 type, strain rate and presence of fluids; Passchier and Trouw, 2005) which also control the morphology
515 and deformation style (e.g. Sibson, 1987; Passchier and Trouw, 2005; Holdsworth et al., 2011). Since we
516 have no independent information about temperature, pressure or other factors, we prefer to discuss our
517 results by referring to three general structural levels on where controlling factors are expected to be rather
518 homogeneous: (a) deep, (2) shallow, and (3) superficial (Fig. 9). Appropriately, the brittle-plastic
519 transition level (BPTL) divides our “deep” and “shallow” structural levels; being in general about 10 km
520 depth, more or less independent of the rock type but strongly temperature-dependent (e.g. Sibson, 1987;
521 Scholz, 2002; Passchier and Trouw, 2005). The BPTL may rise up to ca. 3-4 km depth if fluids (pressure)
522 are present (Holdsworth et al., 2011). The limit between “shallow” and “superficial” structural levels is
523 related to the depth at which deformation becomes not cohesive or discrete on a (set of) single plane (e.g.
524 Sibson, 1987). Thus, structural elements exhibiting no mineral infill or no cohesive material (i.e. slip-
525 surface, cracks and joints) were considered to have developed no deeper than ca. 1 km (“superficial”)

526 depth. On the contrary, those exhibiting some infilling material (e.g. slickenfibers, matrix) were
527 considered to have developed about 1-4 km depth (“shallow”).

528 Accordingly, structural elements of the ESS represent the deepest (and oldest) structural system at
529 Dominga, developed below or close to the BPTL – i.e. about 4 km depth as represented by cataclasites
530 and ultracataclasites. The spatial relationship between these structural elements and the presence of Bt,
531 Mag and Ap – and others –minerals suggest a direct link between the ESS and fluid mobility and arrest
532 (e.g. Sibson, 1987; Caine et al., 1996; Cox et al. 2001) of Fe-rich fluids. Similarly, the geometric
533 arrangement of “shallow” (slip-surfaces and fault-breccias) with respect to “deep” structural elements
534 (ultracataclasites and cataclasites) suggest either an evolution of the system during exhumation towards
535 shallower, more brittle, structural levels and/or a reactivation of the “deep” structural elements under a
536 compatible younger stress field and a structural level closer to the surface.

537 The overall left-lateral structural elements of the ETSS – mostly fault-breccias, cataclasites and
538 other “shallow” and “superficial” structural elements – suggests that it developed at about or above the
539 depth of the BPTL. Here, the different structural elements most probably developed sequentially as the
540 system accommodated to changes to the external stress field and/or to the exhumation conditions. Within
541 the Dominga district, the general geometry of this system seems to be represented almost solely by El
542 Tofo Deformation Band (Fig. 4) which concentrated most of the deformation. The existence of a large,
543 and rather similar, structural element farther east (la Higuera mylonitic zone, cf. Creixell and Arévalo,
544 2009) argues for the occurrence of a km-size, left-lateral, duplex which may be part of the AFS (e.g.
545 Creixell and Arévalo, 2009). However, our field data does not support the existence of a duplex
546 arrangement between El Tofo Deformation Band and La Higuera mylonitic zone, since no kinematically
547 (transfer) connecting structural elements were observed.

548 The ISS most probable developed above the BPTL, on where only exceptions are given by gouge
549 bands (superficial), which may had developed on a later time and on a shallower structural level.
550 Geometrically, this system seems to form a discontinuous duplex arrangement, with E-striking structural
551 elements locally connecting NW-striking ones (Fig. 4). Interestingly, E-striking structural elements of the
552 ISS are similarly oriented with some E-striking structural elements of the ESS, yet these show opposite
553 displacement directions. Thus, it is possible that, at least some, E-striking structural elements developed
554 at the time – and as part of – the ESS, were reactivated due to a different (younger) stress field as part of
555 the ISS.

556 Structural elements (mostly slip-surfaces, fault-breccias, fault-veins and gouge bands) identified as
557 part of the LSS most probably developed above the BPTL, between the depth at where the ISS developed
558 and the surface. Structural elements of the LSS commonly cut and displace all other populations of
559 structural elements, indicating that it is the youngest structural system outcropping in the district.
560 Deformation is rather focused on discrete, subparallel and apparently disconnected structural elements,
561 partially arranged on an *en echelon* geometry (Fig. 4).

562 Overall, it is possible to infer that exhumation at the Dominga district has been more or less
563 steady, from the time of the ESS until the LSS. Such exhumation would be most probable no less than 3-4
564 km when considered the possible initial depth of the ESS.

565

566 8.2. Strain and Stress Fields

567

568 Estimated orientations of principal strain axes indicate that the different structural systems at the
569 Dominga district are dominated by strike-slip deformation, with a general NW-shortening and a NE-
570 stretching (Fig. 10a). However, three concentration maxima of the P and T axes (at ca. 8 and 6%; Fig. 5)
571 were obtained from the analysis of the entire fault-slip data. The largest maxima indicates NW-shortening
572 and NE-stretching, whereas the others indicate dissimilar orientations of the principal strain axes: N-
573 shortening/E-stretching and WNW-shortening/NNE-stretching, respectively. These differences could be
574 the result of the fault-slip data heterogeneity, which prevents a better resolution of the method and
575 therefore isolation of homogeneous, independent, strain fields.

576 Details about the evolution of the strain field can be estimated through kinematic analyses of
577 filtered fault-slip data (Fig. 10). The strain field associated with the ESS was estimated by using both the
578 fault-slip data of this structural system (extracted from the entire fault-slip data set) and the S-C-derived
579 fault-slip data (Fig. 5b, c). To estimate the strain field associated with the other structural systems (ETSS,
580 ISS and LSS) we used the correspondent fault-slip data extracted from the entire fault-slip data set.

581 In general, principal strain axes are subhorizontal for each and all structural systems, thus agreeing
582 with the previous analysis of the entire fault-slip data and supporting the idea of a strike-slip dominated
583 deformation. Nevertheless, estimated orientations of the principal strain axes for each structural system
584 argue for a back-and-forth rotation/shift of the strain field through time (or between structural systems).

585 Despite better estimation on the orientations of the principal strain axes from the S-C-derived
586 fault-slip data, these are fairly similarly oriented to those estimated from the ESS-filtered fault-slip data,
587 both indicating WNW-shortening (P axis) and ENE-stretching (T axis). These principal strain axes are
588 oriented between two of the maximas estimated from the analysis of the entire fault-slip data, arguing
589 against the resolution of the method to process heterogeneous, polyphasic, fault-slip data and the need of
590 fault-slip data filtering. The strain field estimated for the ESS results on right-lateral displacements of
591 NE-striking and nearly pure extension of NW-striking structural elements. These structural elements were
592 observed in the field, corresponding to ultracataclasites and cataclasites and by the Dominga breccia,
593 respectively.

594 Orientations of the principal strain axes estimated for ETSS indicate NNW-shortening and ENE-
595 stretching (Fig. 10d); which would favor left-lateral displacements on the NNE-striking El Tofo
596 Deformation band as well as on structural elements of the ESS. We did not observe left-lateral
597 displacements associated with the structural elements of the ESS, suggesting that this structural system
598 acted passively with respect to the ETSS. The strain field estimated for ETSS is rotated/shifted clockwise
599 (CW) about 40° with respect to that of the ESS; a change that most probable resulted in the abandonment
600 of the right-lateral ESS and the generation of the left-lateral ETSS.

601 For the ISS we estimated a nearly EW-shortening (P axis) and NS-stretching (T axis) (Fig. 10e)
602 strain field; that is rotated/shifted about 70° CCW with respect to that of the ETSS. The strain field
603 associated with the ISS would have favored left-lateral displacements on NW- and EW-striking structural
604 elements, and right-lateral displacements on NNE- and NE-striking ones. Field data supports left-lateral
605 displacements of NW- and EW-striking and right-lateral displacements of NE-striking structural elements
606 but no of NNE-striking ones. This suggests that the strain field associated with the ISS not only generated
607 NW- and EW-striking structural elements on a discontinuous (duplex) geometry, but also it may have
608 reactivated some of the early developed EW-striking structural elements of the ESS but with an opposite
609 sense of displacement.

610 From the ISS to the LSS, once again, the strain field rotated/shifted about 43° CW, resulting in a
611 NW-shortening axis and a NE-stretching, a strain field fairly similarly oriented to that estimated for the
612 ESS (Fig. 10). The strain field associated with the LSS would have favored: (1) left-lateral displacements
613 on NS-striking, (2) right-lateral displacements on NNE-, NE- or EW-striking, and (3) normal
614 displacements on NW-striking, structural elements. However, field data indicates left-lateral

615 displacements solely of NS-striking, *en echelon*, structural elements. Hence, most probably the strain field
616 associated with the LSS did not re-activate any of the previously generated structural elements, driving
617 only a discrete, focused, and not penetrative deformation.

618 Estimated stress field complement and support the deformation history depicted on the strain
619 analysis. Given the advantages of the MIM we estimated homogeneous stress fields based on the analyses
620 over the entire and the S-C-derived fault-slip data sets.

621 Stress field solutions indicate, in general, NW-compression and NE-tension (Fig. 6), a field that is
622 quite similarly oriented when compared to the strain field estimated from the entire fault-slip data (Fig 5).
623 In particular, we estimated four homogeneous stress field solutions that differ both in the orientation of
624 their principal axes and in their associated stress ratios; thus, activating different sets of structural
625 elements. Although none of the estimated solutions can be directly related to a particular structural system
626 on a one-to-one basis (Fig. 6b), the structural elements that each solution activates can be related to
627 particular structural systems.

628 Activity/generation of the structural elements of the ESS is compatible with several of the
629 estimated homogeneous stress fields, yet all these have their principal axes fairly similarly oriented (Fig.
630 6, 10) suggesting a general NW-compression and an NE-tension under a strike-slip regime (e.g. Ritz,
631 1994). Stress ratio values vary from transtensional to transpressional: NE-striking structural elements
632 behave mostly as transtensional, whereas those EW-striking behave as transpressional.

633 In time, the orientation of the stress field rotated/shifted about 15° CW, resulting in abandonment
634 of the ESS and in generation of the ETSS. Given the composite and polyphasic architecture of El Tofo
635 Deformation band and considering its associated stress ratio values, it is possible to argue that the band
636 most probably developed under transtensional conditions during an early stage (perhaps inherited from
637 the previous stress field) followed by transpressional conditions. This resulted in the development of
638 different, independent, discrete – yet continuous and contiguous – deformation bands that concentrated
639 most of the deformation.

640 Structural elements of the ISS (Fig. 4) developed during a period of general NW-compression and
641 NNE-tension, with a significant vertical component of the maximum principal stress axis (Fig. 10) –
642 given by the contribution of solution D. The orientation of this stress field is about 25° CCW
643 rotated/shifted and 30°-40° tilted with respect to the orientation of the stress field estimated for ETSS.
644 Although the structural elements of the ISS were the result of the new (at the time) stress field, some EW-

645 striking structural elements of the ESS may have been reactivated as left-lateral fault-breccias and fault-
646 veins, opposite to right-lateral (ultra)cataclasites of the ESS. Stress ratio values associated with the ISS
647 indicate a transpressional-transtensional behavior of the system. Here, NW- to NNW-striking structural
648 elements are related to transtensional stress ratio values, whereas those striking NW to EW are mostly
649 related to transpressional ones.

650 The orientation of the stress field associated with the structural elements of the LSS indicates
651 strike-slip regime with a NW-compression and a NE-tension. The orientation of this stress field is
652 rotated/shifted about 10° CW with respect to that estimated for the, previous, ISS. Stress ratio values for
653 the LSS are mostly transpressional, yet some few structural elements may have behaved as transtensional.

654 Overall, estimated strain and stress fields indicate a general NW-SE trending
655 shortening/compression and a NE-SW trending stretching/tension (Fig. 5, 6, 10) that experienced slight
656 changes in orientation and between transtensional and transpressional characteristics. Principal axes of
657 strain and stress fields estimated for each structural system are not coaxial, supporting the idea of an
658 overall strike-slip regime, simple-shear dominated deformation during the activity of all identified
659 structural systems. Differences in the orientation of both strain and stress fields among structural systems
660 also argue for a back-and-forth rotation/shift through time; CW rotations are associated with
661 transpressional conditions whereas CCW are with transtensional ones (Fig. 10c). In all cases, it seems that
662 rotation/shift of the strain/stress field resulted in the abandonment of a particular structural system and the
663 development of a new, independent, one.

664 Rotation of tectonic blocks has been proposed for the northern part of the El Salado segment of the
665 AFS (e.g. Taylor et al., 1998; Forsythe and Chisholm, 1994; Rojas et al., 1994; Beck, 1998), which may
666 be related to rotations/shifts of the orientations of the strain/stress fields estimated at the Dominga district.
667 Although not reported as a rotation/shift of tectonic blocks or of strain/stress fields, Scheuber and
668 González (1999), argue for relaxation of the overriding (South American) plate – between ca. 155 and ca.
669 140 Ma – during a period of overall SE-trending subduction, prior to the initiation of the AFS (e.g. Coira
670 et al., 1982; Scheuber and Gonzalez, 1999; Grocott and Taylor, 2002). Accordingly, this would have
671 triggered the development of right-lateral NE-striking structural elements. Given the probable pre-AFS
672 age and the similarities in orientation between the structural elements of the ESS and those proposed by
673 Scheuber and Gonzalez (1999), it is most probable that these correlate. This idea is supported by available
674 geochronological constraints. The activity of the ESS is constrained by the rocks of the Punta del Cobre

675 Formation (>140 Ma; Creixell and Arévalo, 2009), by our ca. 127 Ma (U-Pb) age obtained from Ap
676 crystals as well as by the proposed age for the initiation activity of the AFS at ca. 125 Ma (Scheuber and
677 González, 1999; Grocott and Taylor, 2002). However, and given the nearly 127 Ma Re-Os age obtained
678 from Molybdenite crystals, it is most probable that the ESS ended its activity before or close to ca. 127
679 Ma (Fig. 11).

680 From the ESS to the ETSS, estimated strain/stress fields rotated/shifted CW about 40° and 15°,
681 respectively (Fig. 10). Such rotation/shift could resulted from either rotation of discrete (fault-bounded)
682 tectonics blocks – and therefore of the strain/stress fields that they recorded – or a simple rotation/shift of
683 the overall stress/strain field most probable controlled by the convergence direction of the subducting
684 plate (e.g. Scheuber and González, 1999; Grocott and Taylor, 2002). If rotation of tectonic blocks –
685 between the major lineaments of El Tofo deformation band and La Higuera Mylonitic Zone (e.g. Creixell
686 and Arévalo, 2009) – is the cause, then the ESS would have experienced a CCW rotation of, at least, 15°.
687 If so, then the ESS would had a general strike of N70°-90°E before the development of the ETSS. Based
688 on paleomagnetic analyses in the northern part of the El Salado segment of the AFS, Taylor et al. (1998)
689 proposed a ca. 10° rotation of the Mesozoic arc at ca. 132-125 Ma, an age within that estimated for the
690 activity of the ESS (Fig. 11). On the contrary, if rotation/shift of the strain and stress fields resulted from
691 a rotation/shift of the overall subduction convergence, then the ESS would have acted as a passive
692 element, ergo being only left-laterally disrupted and displaced by the ETSS.

693 The overall N20°-40°E trend of the ETSS is roughly subparallel to that of the AFS (e.g. Brown et
694 al, 1993) and both show similar displacement (left-lateral) direction, suggesting a spatial and temporal
695 affinity (e.g. Coira et al., 1982; Scheuber and Gonzalez, 1999; Grocott and Taylor, 2002). Hence, it is
696 highly possible that the ETSS is part (local) of the AFS, perhaps representing a splayed off arm of it. This
697 implies that the time of activity of the ETSS and the AFS can be correlated, constraining the activity of
698 the ETSS between ca. 125 to ca. 90 Ma (Scheuber and González, 1999; Grocott and Taylor, 2002).

699 Once more, we estimated a CCW rotation/shift of the strain/stress fields from the ETSS to the ISS,
700 which could have resulted from rotation of discrete tectonic blocks or from shift/rotation on the
701 convergent direction of the subducting plate. CCW rotation of tectonic blocks or of structural elements of
702 the AFS has not been reported, to the best of our knowledge, for any of its segments. Thus, the estimated
703 ca. 71° and 25° CCW rotation/shift of the strain and stress fields, respectively, estimated for the change
704 from the ETSS to the ISS structural systems is most probably related to a shift in the convergence

705 direction of the subducting plate. We agree with the general view that these NW-striking structural
706 elements (ISS) are the result of a change in the general tectonic configuration of the South American Arc
707 (e.g. Mpodozis and Ramos, 1990; Taylor et al., 1998) rather than to (a local) rotation of tectonic blocks.
708 The shift from ETSS to the ISS most probably occurred after the cease of the activity of the AFS (ca. 90
709 Ma) and lasted until reconfiguration ended, i.e. ca. 80 Ma (Fig. 11) (e.g. Mpodosiz and Ramos, 1990;
710 Grocott and Taylor, 2002).

711 A further CW rotation/shift of 43° and of 10° CW of the strain and stress fields, respectively,
712 occurred between the development of the ISS and of the LSS (Fig. 10). Since structural elements of the
713 ISS are cut and displaced by those of the LSS, the rotation/shift most probably occurred after the cease of
714 the ISS. Unfortunately, no geochronological constraints are available, yet reported Cenozoic CW
715 rotations in the forearc (e.g. Arriagada et al., 2006; Roperch et al., 2006; Taylor et al., 2007) could be
716 related to the activity of the LSS. In such case, the LSS developed sometime after 80-40 Ma.

717

718 8.3. Alteration/Mineralization Stages

719

720 Identified mineral paragenetic assemblages depict the arrest of fluids and argue for a discrete
721 evolution towards lower temperature mineral phases. The four alteration/mineralization stages defined
722 here (labeled stages I to IV on Fig. 7) roughly correlate with similar stages defined and identified on
723 several Fe-rich deposits in northern Chile (e.g. Arévalo et al., 2006; Marschik and Fontboté, 2001;
724 Benavides, 2007).

725 Alteration/mineralization stage I – marked by the occurrence of fine-grained Bt and Mag crystals
726 together with Act, Py and rare Ttn – is similar to alteration/mineralization mineral assemblages described,
727 for example, in Candelaria (e.g. Arévalo, 2006), El Romeral (Bookstorm, 1977), Mantoverde (Benavides,
728 2007) and for the Candelaria-Punta del Cobre district in general (Marschik and Fontboté, 2001). At a
729 regional scale, this alteration/mineralization has been interpreted as a result of a widespread
730 metasomatism due to the emplacement of plutonic bodies during the Late Jurassic-Early Cretaceous (e.g.
731 Arévalo, 2006; Bookstorm, 1977; Taylor et al., 1998; Marschik and Fontboté, 2001; Benavides et al.,
732 2007; Fig. 11).

733 The occurrence of coarse- to medium-grained Mag, Bt and, locally, Act and Py crystals as: matrix
734 of hydrothermal breccias, constituent material of (foliated) ultracataclasites and cataclasites, vein filling

735 material together with Qtz crystals, and as strata-like Fe-rich bodies that follow the strata of the rocks of
736 the Punta del Cobre Formation, marks the beginning of alteration/mineralization stage II (Fig. 7) which
737 corresponds to the main Fe-mineralization at Dominga. Ap crystals seem to have crystallized at a medium
738 to later time within stage II, as evidence by crosscutting relations between veins filled with Ap, Ap+Mag
739 and hydrothermal breccias with an Act-Ap-rich matrix. Accordingly, we prefer to divide our stage II into
740 sub-stages IIa and IIb, defined by the lack and occurrence of Ap crystals, respectively (Fig. 7, 11). Similar
741 paragenetic assemblages have been described for other Fe-rich deposits in the region, including
742 Candelaria (Marschik and Fontboté, 2001), Cerro Negro (Vivallo et al., 1995), El Romeral-Algarrobo
743 (Bookstrom, 1977; Nyström and Henríquez, 1994), Fresia and Carmen (Bonson, 1996), Productora (Ray
744 and Dick, 2002) and Panulcillo (Correa, 2000). For example, at Candelaria, this paragenetic assemblage
745 has been defined as “Iron Oxide Stage”, representing part of the ore mineralization and partly hosted on
746 NE-striking structural elements (Marschik and Fontboté, 2001; Arévalo et al., 2006).

747 Alteration/mineralization stage III (defined by the occurrence of Kfs, Ep and coarse-to medium-
748 grained Mag crystals) was mostly observed as filling material of veins subparallel to (foliated)
749 ultracataclasites and cataclasites, and to veins filled with Mag and Mag-Act. Crosscutting relations
750 suggests a later growth of Anh-Aln-Vrm crystals, most probably coeval or pene-contemporaneous with
751 Ccp-Py-Mo crystallization. Hence, we prefer to divide our alteration/mineralization stage III into sub-
752 stages IIIa and IIIb, defined by the occurrences of Kfs±Ep and Anh-Aln-Vrm-Ccp-Py-Mo, respectively.
753 Structural elements displaying an Anh-Aln-Vrm-related paragenetic assemblage are both subparallel to
754 the structural elements of the ESS and of the ETSS. Moreover, relicts of Kfs filled veins are included into
755 some fault-breccias of the El Tofo Deformation band. Crosscutting relations between Kfs-Ep and Anh-
756 Aln-Vrm paragenetic assemblages are in places opposite, yet both are post-Act crystals (stage IIa), and
757 pre-Hem and/or Cal-rich (stage IV) mineral assemblages. This suggests that stage III occurred between
758 the transition from the ESS to the ETSS, probably related to the transtensional activity of both systems.

759 Cu-related mineralization in Fe-rich deposits in northern Chile corresponds mostly to the
760 occurrence of Ccp, and described as accompanied by Aln and light REE in the deposits of Productora and
761 Santa Inés (Ray and Dick, 2002). At Productora, Osterman (1997), argues for a Ccp mineralization stage,
762 coeval (or at least pene-contemporaneous) with the occurrence of Kfs and Ep crystals. Also, for the
763 deposit of El Romeral, Bookstrom (1977) associated a Py-Ccp-Ep paragenetic assemblage to the observed
764 Cu-mineralization; whereas at Candelaria, Marschik and Fontboté (2001) and Marschik et al. (2000),

765 argue that the main Cu-mineralization is associated with the occurrence of Aln and Anh crystals that grew
766 after the main Fe-mineralization stage, i.e during the activity of the AFS.

767 Alteration/mineralization stage IV (Hem, Py, Ccp, oxidized Ccp and Cal; Fig. 7, 11) mostly occurs
768 as filling material of veins and as part of the matrix of hydrothermal- and fault-breccias. A similar
769 paragenetic association has been described for the deposits of Teresa de Colmo (Bonson, 1996) and
770 Candelaria (Ruiz et al., 1965; Marschik and Fontboté, 2001), and interpreted as the end of the hypogene
771 mineralization. However, the presence of oxidized forms of Ccp and the presence of Hem (specularite)
772 suggest at least a slight degree of supergene alteration.

773 The paragenetic assemblages identified at Dominga argue for a decreasing temperature of the
774 mineralizing fluids, evidenced by the change from Mag-Act-Bt-rich towards Hem-Ep-Cal-rich
775 assemblages (Fig. 7). Previously published geochemical analyses carried on mineralogically similar Fe-
776 rich deposits in the region also argue for a decreasing temperature of the mineralizing fluids, from at least
777 600°-500°C (stage I and II) to 470°-340°C (stage III) and down to ca. 230°C (stage IV) (Marschik and
778 Fontboté, 2001).

779 Alteration/mineralization stages similar to those defined here have been dated using several
780 methods and materials, giving ages between 131,0±0,1 Ma (at Carmen Sur; Gelcich et al., 2005) and ca.
781 111,0 Ma (at Candelaria; Arévalo et al., 2006) (Fig. 11). At Dominga, paragenetic assemblage stage I
782 grew onto the rocks of the Punta del Cobre Formation and of the Porphyric Dioritic Complex, which are
783 no younger than 140-139 Ma (Creixell and Arévalo, 2009) (Fig. 11). This constraints the probable
784 beginning of stage I, yet it could have started as early as ca. 149 Ma when considering Ar-Ar (Act)
785 geochronological data from the Cordón de Véliz area (Fig. 11) (Vivallo et al., 2008). The end of stage I is
786 here constrained by the activity of the ESS, since its structural elements show relicts of this paragenetic
787 assemblage.

788 Although no direct constraints for the beginning of stage IIa are available, it can be argued that it
789 started after stage I, i.e. ca. 140-139 Ma, which correlates with the end of the relaxation of the upper plate
790 proposed by Scheuber and González (1999). Despite this, the occurrence of Ap crystals (stage IIb) can be
791 correlated with similar mineral occurrences at Carmen Sur, dated ca. 131 Ma (U-Pb, Ap) (Gelcich et al.,
792 2005), as well as by our ca. 127 Ma U-Pb (Ap) age (Fig. 11).

793 Age constraints for stage III are given by our U-Pb (Ap) and Re-Os (Molybdenite)
794 geochronological data, and by similar Re-Os dating at Candelaria (Mathur et al., 2002) (Fig. 11). Stage

795 IIIa must have started at ca. 127 Ma, slightly after or shortly overlapped with Ap crystallization. Stage
796 IIIb started just after ca. 127 Ma, lasting until ca. 114 Ma, assuming that the occurrences of Molybdenite
797 at Dominga and at Candelaria deposits resulted from correlated alteration/mineralization processes (Fig.
798 11).

799 Alteration/mineralization stage IV is unrelated to the ETSS (and therefore to the activity of the
800 AFS) but to the ISS. As argued before, the ISS started after the cease of the AFS, i.e after ca. 90 Ma (i.e.
801 Scheuber and González, 1999; Grocott and Taylor, 2002), and lasted until reconfiguration of the South
802 American Arc ended at ca. 80 Ma (e.g. Mpodozis and Ramos, 1990; Taylor et al., 1998). Stage IV then
803 would have lasted at most for about 10 m.y., from ca. 90 to ca. 80 Ma (Fig. 11).

804

805 8.4. Tectono-Metallogenic Evolution

806

807 As shown, alteration/mineralization stage I corresponds to a widespread, regional, metasomatic
808 event, hence, unrelated to any identified structural system at Dominga or elsewhere among Fe-rich
809 deposits in the region. On the contrary, the spatial orientation and locale of Mag-rich, Ap-rich and Mag-
810 Act-rich veins and strata-like bodies, together with similar mineral contents in the matrix of
811 ultracataclasites and cataclasites and hydrothermal breccias indicate a direct link between the ESS and
812 stage II (Fig. 11, 12). Hence, we can argue that the emplacement of the main Fe-rich mineralization at
813 Dominga was controlled by and occurred during the transtensional activity of the ESS.

814 The occurrence of veins filled with Ep and Kfs subparallel to the structural elements of the ESS, as
815 well as the presence of Ep as constituent of the matrix of hydrothermal breccias suggest that stage IIIa
816 occurred during the (waning?) activity of the ESS. The occurrence of Ep-related paragenetic mineral
817 assemblages (such as Vrm-Aln-Anh) as part of the matrix of hydrothermal breccias of some of the
818 structural elements of El Tofo Deformation Band as well as filling material of veins subparallel to the
819 structural elements of the ESS and of the ETSS suggest that stage IIIb was contemporaneous with the
820 both structural systems, possibly marking a transition stage between them. This argues that the main Fe-
821 Cu-mineralization stage (III) is most probably associated with the transtensional activity of the ESS and
822 with the earliest – most probable also transtensional – activity of ETSS. This later process of
823 alteration/mineralization (stage IIIb) seems to correlate with various Cu-mineralizations identified on

824 other Fe-Cu-rich deposits in the region (e.g. Arévalo et al., 2006; Mathur et al., 2002; Marschik and
825 Fontboté, 2001; Arévalo et al., 1999).

826 A late Fe-Cu-rich mineralization, represented by the mineral assemblages of stage IV, was
827 emplaced during the activity of the ISS, after the cease of ETSS and, regionally, of the NS- to NNE-
828 striking AFS (e.g. Grocott and Taylor, 2002; Taylor et al., 1998). This is supported by the conspicuous
829 occurrence of Hem and Cal, both accompanied by Ccp, as mineral infill in veins, hydrothermal breccias
830 and composite structural elements with strikes of about N30°-60°W (Fig. 2, 12).

831 Field-based observations indicate that the structural elements of the LSS are unrelated to any
832 alteration/mineralization observed at Dominga. No veins of specific alteration/mineral assemblages were
833 found either subparallel or included into these structural elements. This activity of this system thence only
834 modified the overall geometry of the deposit, via left-lateral, strike-slip deformation (Fig. 4, 12).

835

836 9. Conclusions

837

838 The occurrence of a Fe-Cu-mineralization at Dominga is spatially, genetically and tectonically
839 associated with four different and independent structural systems. Strain and stress analyses performed
840 over fault-slip data from a variety of structural elements indicate a rotation/shift of these fields during the
841 deformation history of the Dominga deposit. The emplacement and arrest of Fe-Cu-rich fluids and the
842 generation of the Dominga Fe-rich deposit pre-, syn- and post-dates the activity of the AFS (Fig. 11, 12).

843 Our results can be summarized as follow:

- 844 • There is a background, regional, alteration/mineralization represented by disseminated, yet pervasive,
845 occurrence of fine-grained Bt-Mag (-Py-Act-Ttn) crystals (stage I) in the rocks of the Punta del Cobre
846 Formation and in the Porphyric Dioritic Complex.
- 847 • The ESS corresponds to a right-lateral duplex arrangement of deep seated (3-4 km depth) structural
848 elements with preferential strikes between N50°-70°E and N80°-100°E. The main activity of this
849 system was between ca. 139 and ca. 125 Ma, with a general transtensive regime, which controlled the
850 mobility and arrest of Fe-rich alteration/mineralization fluids.
- 851 • The main Fe-rich mineralization/alteration at the Dominga deposit corresponds to the occurrence of
852 coarse- to medium-grained Mag-Bt-Act-Ap paragenetic assemblage (stage II), spatially associated

853 with the strata of the Punta del Cobre Formation, with the Porphyric Dioritic Complex and with
854 structural elements of the ESS such as foliated ultracataclasites and foliated and non-foliated
855 cataclasites, veins and hydrothermal breccias. Geochronological data (Ap, U-Pb) indicates an age of
856 ca. 127.0 ± 15.0 Ma for the Ap crystallization (stage IIb).

- 857 • A second mineralization/alteration, related to the ESS, corresponds to the occurrence of Kfs and Ep-
858 rich (stage IIIa) whereas a later Anh-Aln-Vrm-Ccp-rich (IIIb) alteration/mineralization is related to
859 both the ESS and the ETSS. These two stages (IIIa and IIb) represent a second Fe-Cu-rich
860 alteration/mineralization at the Dominga district. Geochronological data (Molybdenite, Re-Os)
861 indicates an age of ca. 127.0 ± 0.65 Ma for alteration/mineralization stage IIIb). The $^{206}\text{Pb}/^{238}\text{U}$ age in
862 apatite of 127 ± 15 Ma is considered the best estimation to the hydrothermal apatite breccia, and most
863 probably older than the molybdenite age.
- 864 • A CW rotation/shift of both strain and stress fields caused the abandonment of the structural elements
865 of the ESS and the development of those of the ETSS (which correlates with the AFS). The ETSS
866 developed under transtensional/tranpressional tectonic conditions, at a depth of about the BPTL (i.e. 3-
867 4 km) and above. Deformation was concentrated onto a composite structural element with a nearly
868 $\text{N}20^\circ\text{-}40^\circ\text{E}$ strike preferential direction. Correlation with available geochronological data suggests that
869 this system was active between ca. 125 and ca. 90 Ma.
- 870 • The ETSS, during an initial transtensive phase, most probably controlled the ascent and emplacement
871 of Fe-Cu-rich fluids (stage IIIb). However, a change towards a transpressive tectonic phase resulted in
872 the cease of alteration/mineralization stage IIIb at Dominga. The tectonic activity of ETSS also
873 changed the initial geometry of the deposit by left-lateral disruption (and perhaps some minor
874 rotation) of, fault-bounded, tectonic blocks.
- 875 • A CCW rotation/shift of the strain and stress fields, resulted from the change of the convergence
876 subduction direction, caused the cease of tectonic activity on ETSS and the development of an
877 arrangement of a series of $\text{N}30^\circ\text{-}60^\circ\text{W}$ and $\text{N}80^\circ\text{-}100^\circ\text{E}$ striking structural elements that define the ISS.
878 This later system developed (between 90 and 80 Ma) at a shallower depth with respect to the
879 structural elements of the ESS, yet it probably was similar to the depth at which the ETSS developed.
- 880 • The transtensional activity of the ISS was accompanied by a late Fe-Cu-rich mineralization (stage IV),
881 represented by the occurrence of Hem and Cal (together with oxidized Ccp). Similar to the role played

882 by ETSS, the ISS controlled the emplacement of a late alteration/mineralization, yet it also changed
883 the geometry of the deposit via left-lateral disruption of fault-bounded tectonic blocks.

884 • Finally, a CW rotation/shift of the strain and stress fields resulted in the abandonment of the ISS and
885 the development of the LSS. The structural elements of this later system most probably developed at a
886 shallow to superficial depth and were were, in any case, active post any identified
887 alteration/mineralization at Dominga, thus being probably Cenozoic in age and unrelated to the main
888 tectono-metallogenic evolution of the Dominga deposit. Thence, the LSS only modified the, already
889 disrupted, geometry of the deposit.

890

891 Acknowledgements

892

893 We would like to thank all personnel at Dominga site for their valuable help during field
894 campaigns. Special thanks to M. Vivanco, for his comments and suggestions in the field that helped to
895 unravel the complex tectono-metallogenic processes at Dominga. This work was supported by a joint
896 project venture between Andes Iron SpA and the Direction of Research and Science (DICTUC) of the
897 Pontifical Catholic University of Chile and it is a contribution to Millennium Science Initiative
898 NC130065.

899

900

901 REFERENCES

902

903 Angelier, J (1994) Fault slip analysis and paleostress reconstruction. In: Hancock, P. (ed.) Continental
904 Deformation. Pergamon press, UK, pp 53-100.

905 Arévalo, C (1999) The coastal Cordillera-Precordillera boundary in the Copiapó area, northern Chile and
906 the structural setting of the Candelaria Cu-Au ore deposit. Ph.D. dissertation, Kingston University

907 Arévalo, C, Grocott, J, Martin, W, Pringle, M, Taylor, G (2006) Structural Setting of the Candelaria Fe
908 Oxide Cu-Au Deposit, Chilean Andes (27°30`S). *Economic Geology* 101: 819-841.

909 Arriagada, C, Roperch, P, Mpodozis, C, Fernandez, R (2006) Paleomagnetism and tectonics of the
910 southern Atacama Desert (25-28 degrees S), northern Chile. *Tectonics* 25(4): TC4001.

911 Beck, M (1998) On the mechanism of crustal block rotation in the central Andes. *Tectonophysics* 299:
912 75-92

913 Benavides, J, Kyser, T, Clark, A, Oates, C, Zamora, R, Tarnovschi, R, Castillo, B (2007) The Mantoverde
914 Iron Oxide-Copper-Gold District, III Región, Chile: The Role of Regionally Derived, Nonmagmatic
915 Fluids in Chalcopyrite Mineralization. *Economic Geology* 102: 415-440.

916 Bonson, C, Grocott, J, Rankin, A, (1996) A structural model for the development of Fe-Cu mineralisation
917 within the Atacama Fault System, (25°00`S-27°15`S), Northern Chile. Third ISAG, St. Malo, France:
918 671-674.

919 Bookstrom, A (1977) The magnetite deposits of El Romeral, Chile. *Economic Geology* 72: 1101-1130.

920 Bott, M (1959) The mechanisms of oblique slip faulting. *Geological Magazine* 96: 109-117.

921 Brown, M, Diaz, F, Grocott, J (1993). Displacement history of the Atacama Fault System 25°-27°S,
922 northern Chile. *Geological Society of America Bulletin* 105: 1165-1174.

923 Butler, R (1992). *Paleomagnetism: Magnetic domains to geologic terranes*, Blackwell Scientific
924 Publications, Boston..

925 Caine, J, Evans, J, Forster, C (1996) Fault zone architecture and permeability structure. *Geology* 24:
926 1125-1128.

927 Cembrano, J, Garrido, I, Marquardt, M (2009) Tectonic setting of IOCG deposits in the Central Andes:
928 Strike-slip-dominated deformation. XII Congreso Geológico Chileno, Santiago: S9_043

929 Coira B, Davidson J, Mpodozis C, Ramos V (1982) Tectonic and magmatic evolution of the Andes of
930 Northern Argentina and Chile. *Earth Science Reviews* 18: 303-332.

- 931 Correa, A (2000) Geología del Yacimiento Fe-Cu Teresa del Colmo, Región de Antofagasta, Chile. 9th
932 Congreso Geológico Chileno v2: 102-106.
- 933 Cox, S, Knackstedt, M, Braun, J (2001) Principles of structural control on permeability and fluid flow in
934 hydrothermal systems. Society of Economic Geologist Reviews 14: 1-24.
- 935 Creixell, C, Arévalo, C (2009) Geología del Cuadrángulo El Tofo, Región de Coquimbo.
936 SERNAGEOMIN, Gobierno Regional de Coquimbo. mapa a escala 1:50.000. Santiago.
- 937 Creixell, C, Arévalo, C, Fanning, M (2009) Geochronology of the cretaceous magmatism from the
938 Coastal Cordillera of north-central Chile (29°15` to 29°30`S): metallogenic implications. XII Congreso
939 Geológico Chileno.
- 940 Doblas, M (1998) Slickenside kinematic indicators. Tectonophysics 295: 187-197.
- 941 Espinoza, S (1984) Le rôle du Crétacé inférieur dans la métallogénèse de la ceinture ferrifère d'Atacama-
942 Coquimbo, Chili. Doctoral thesis, l'Université Pierre et Marie Curie, Paris.
- 943 Espinoza, S (1990) The Atacama-Coquimbo ferriferous belt, northern Chile. In: Fontboté, L, Amstutz, G,
944 Cardozo, M, Cedillo, E, Frutos, J (eds) Stratabound ore deposits in the Andes. Berlin, Springer –
945 Verlag, pp 353–364.
- 946 Federico, L, Crispini, L, Capponi, G (2010) Fault-slip analysis and transpressional tectonics: A study of
947 Paleozoic structures in northern Victoria Land, Antarctica. Journal of Structural Geology 32: 667-684.
- 948 Forsythe, R, Chisholm, L (1994) Paleomagnetic and structural constraints on the rotation in the northern
949 Chilean Coast Ranges. Journal of South American Earth Sciences 7: 279–295.
- 950 Geijer, P (1931) The iron ores of the Kiruna type. Sveriges Geologiska Undersökning C367, 39 p.
- 951 Gelcich, S, Davis, D, Spooner, T (2005) Testing the apatite-magnetite geochronometer: U-Pb and
952 ⁴⁰Ar/³⁹Ar geochronology of plutonic rocks, massive magnetite-apatite tabular bodies, and IOCG
953 mineralization in Northern Chile. Geochimica and Cosmochimica Acta 69(13): 3367-3384.
- 954 Griffin, W, Powell, W, Pearson, N, O'Reilly, S (2008) GLITTER: data reduction software for laser
955 ablation ICP-MS. In: Sylvester, P. (ed), Laser Ablation-ICP-MS in the Earth Sciences. Mineralogical
956 Association of Canada Short Course Series Volume 40 (Appendix 2): 204-207.
- 957 Grocott J, Taylor G (2002) Magmatic arc fault system, deformation partitioning and emplacement of
958 granitic complexes in the Coastal Cordillera, north Chilean Andes (25°30'S to 27°00'S). Journal of
959 the Geological Society of London 159: 425–442.

960 Holdsworth, R, van Diggelen, E, Spiers, C, de Bresser, J, Walker, R, Bowen, L (2011) Fault rocks from
961 the SAFOD core samples: Implications for weakening at shallow depths along the San Andreas Fault,
962 California. *Journal of Structural Geology* 33: 132-144.

963 Ludwig, K. (2003) User's Manual for Isoplot 3.00 a Geochronological Toolkit for Microsoft Excel.

964 Marrett, R., Allmendinger, R.W. (1990) Kinematic analysis of fault-slip data. *Journal of Structural*
965 *Geology* 12: 973-986.

966 Marschik, R., Fontboté, L. (2001) The Candelaria-Punta del Cobre iron oxide Cu-Au (-Zn-Ag). *Economic*
967 *Geology* 96: 179-1826.

968 Marschik, R., Leveille, R.A., Martin, W. (2000) La Candelaria and the Punta del Cobre district, Chile:
969 Early Cretaceous iron oxide Cu-Au(-Zn-Ag) mineralization. In: Porter, T.M. (ed.): *Hydrothermal iron-*
970 *oxide coppergold & related deposits: A global perspective: Adelaide, Australian Mineral Foundation,*
971 *pp 163–175.*

972 Marschik, R., Singer, B.S., Munizaga, F., Tassinari, C., Moritz, R., Fontboté, L. (1997) Age of Cu (-Fe)-
973 Au mineralization and thermal evolution of the Punta del Cobre district, Chile. *Mineralium Deposita*
974 32: 531–546.

975 Mathur, R.D., Marschik, R., Ruiz, J., Munizaga, F., Martin, W. (2002) Age of mineralization of the
976 Candelaria iron oxide Cu-Au deposit, and the origin of the Chilean iron belt based on Re-Os isotopes.
977 *Economic Geology* 97: 59-71.

978 Ménard, J. (1986) Un modèle métasomatique pour les gisements de la Ceinture de fer du Chili. *Académie*
979 *de Sciences [Paris] Comptes Rendus des Séances.II* 302: 775-778.

980 Mpodozis, C., Ramos, V.A. (1990) The Andes of Chile and Argentina. In: Ericksen, G.E., Pinochet,
981 M.T.C., Reinemund, J.A. (eds.) *Geology of the Andes and its relation to hydrocarbon and mineral*
982 *resources. Houston, Texas, Circum-Pacific Council for Energy and Mineral Resources, pp. 59–90.*

983 Nyström, J.O., Henríquez, F. (1994) Magmatic features of iron ores of the Kiruna type in Chile and
984 Sweden: Ore textures and magnetite geochemistry. *Economic Geology* 89: 820–839.

985 Osterman, C. (1997) Mineralogical notes on the Productora project, Region III, Chile. Unpublished
986 report, General Minerals Corporation, May 1997, 8 pages.

987 Otsubo, M.; Yamaji, A. (2006) Improved resolution of the Multiple Inverse Method by eliminating
988 erroneous solutions. *Computers and Geosciences* 32: 1221-1227.

- 989 Oyarzún, J, Frutos, J. (1984) Tectonic and petrological frame of the Cretaceous iron deposits of north
990 Chile. *Mining Geology* 34: 21-31.
- 991 Park, C.F., Jr. (1972) The iron ore deposits of the Pacific basin. *Economic Geology* 67: 339-349.
- 992 Passchier, C.W., Trouw, R.A.J. (2005) *Microtectonics*. Berlin-Heilderberg, Springer-Verlag, 366 pp.
- 993 Pearce, N.J.G., Perkins, W.T., Westgate, J.A., Gorton, M.P., Jackson, S.E., Neal, C.R., Chenery, S.P.
994 (1997) A compilation of new and published major and trace element data for NIST SRM 610 and
995 NIST SRM 612 glass reference materials. *Geostandard Newslett.* 21: 115–144
- 996 .Petit, J. (1987) Criteria for the sense of movement on fault surfaces in the brittle rocks. *Journal of*
997 *Structural Geology* 9: 597–608.
- 998 Ray, G.E., Dick, L.A. (2002) The Productora prospect in North-Central Chile: An example of an intrusion
999 related, Candelaria Type Fe-Cu-Au Hydrothermal System. In: Porter, T.M. (Ed.) *Hydrothermal Iron*
1000 *Oxide Copper-Gold & Related Deposits: A Global Perspective, Volume 2*. PGC Publishing, Adelaide,
1001 Australia, pp. 131-151.
- 1002 Ritz, J. (1994) Determining the slip vector by graphical construction: use of a simplified representation of
1003 the stress tensor. *Journal of Structural Geology* 16(5): 737-741.
- 1004 Rojas, C., Beck, M., Burmester, R., Cembrano, J., Hervé, F. (1994) Paleomagnetism of the Mid-Tertiary
1005 Ayacara Formation, southern Chile: counterclockwise rotation in a dextral shear zone. *Journal of*
1006 *South American Earth Sciences* 7: 45–56.
- 1007 Roperch, P., Sempere, T., Macedo, O., Arriagada, C., Fornari, M., Tapia, C., Garcia, M., Laj, C. (2006)
1008 Counterclockwise rotation of late Eocene-Oligocene fore-arc deposits in southern Peru and its
1009 significance for oroclinal bending in the central Andes. *Tectonics* 25: TC3010.
- 1010 Ruiz, C., Peebles, F. (1988) *Geología, distribución y génesis de los yacimientos metalíferos chilenos*.
1011 Santiago, Editorial Universitaria, 334 pp.
- 1012 Ruiz, C., Aguirre, L., Corvalan, J., Klohn, C., Klohn, E., Levi, B. (1965) *Geología y yacimientos*
1013 *metalíferos de Chile: Instituto de Investigaciones Geológicas [Chile]*, 386 p.
- 1014 Selby, D., Creaser, R. (2001) Re-Os Geochronology and systematics in molybdenite from the Endako
1015 Porphyry Molybdenum Deposit, British Columbia, Canada. *Economic Geology* 96:197-204.
- 1016 Scheuber, E., González, G. (1999) Tectonics of the Jurassic-Early Cretaceous arc of the north Chilean
1017 Coastal Cordillera (22°-26°S): A story of crustal deformation along a convergent plate boundary.
1018 *Tectonics* 18: 895-910.

- 1019 Scheuber, E., Andriessen, P. (1990) The kinematic and geodynamic significance of the Atacama Fault
1020 Zone, northern Chile. *Journal of Structural Geology* 12: 243-250.
- 1021 Scholz, C. (2002) *The Mechanics of Earthquakes and Faulting*. Cambridge Press, second edition,
1022 Cambridge, UK, 470pp.
- 1023 Sibson, R.H. (1987) Earthquake rupturing as a mineralizing agent in hydrothermal systems. *Geology* 15:
1024 701-704.
- 1025 Sillitoe R. H. (2003) Iron oxide-copper gold deposits: an Andean review. *Mineralium Deposita* 38: 787-
1026 812.
- 1027 Sippel, J., Scheck-Wenderoth, M., Reicherter, K., Mazur, S. (2009) Paleostress states at the south-western
1028 margin of the Central European Basin System – Application of fault slip analysis to unravel polyphase
1029 deformation pattern. *Tectonophysics* 470: 129-146.
- 1030 Sperner, B., Zweigel, P. (2010) A plea for more caution in fault-slip analysis. *Tectonophysics* 482: 29-41.
- 1031 Tauxe, L. (1998) *Paleomagnetic Principles and Practice*. Modern Approaches in Geophysics. Kluwer
1032 Academic, Amsterdam.
- 1033 Taylor, G., Grocott, J., Pope, A., Randall, D. (1998) Mesozoic faults systems, deformation and fault block
1034 rotation in the Andean forearc: a crustal-scale strike-slip duplex of the Coastal Cordillera of northern
1035 Chile. *Tectonophysics* 299: 93-109.
- 1036 Taylor, G., Grocott, J., Dashwood, B., Gipson, M., Arevalo, C. (2007) Implications for crustal rotation
1037 and tectonic evolution in the central Andes fore arc: New paleomagnetic results from the Copiapo
1038 region of northern Chile, 26°-28°S: *Journal of Geophysical Research-Solid Earth* 112: B01102.
- 1039 Thomson, S.N., Gehrels, G.E., Ruiz, J., Buchwaldt, R. (2012) Routine low-damage U-Pb dating of apatite
1040 using laser ablation-multicollector-ICPMS. *Geochemistry, Geophysics, Geosystems* 13: Q0AA21,
1041 doi:10.1029/2011GC003928.
- 1042 Ullrich, T. D., Clark, A. H. (1999) The Candelaria copper-gold deposit, Region III, Chile: Paragenesis,
1043 geochronology and fluid composition. In: Stanley, C.J. et al. (eds.) *Mineral Deposits: Processes to*
1044 *Processing*. Rotterdam, Balkema, pp. 201–204.
- 1045 Veloso, E., Anma, R., Yamaji, A. (2009) Heterogeneous Paleostress Regimes Recorded on the Taitao
1046 Ophiolite (Southern Chile), Implications for Ophiolite Emplacement and Effects of the Subduction of
1047 the Chile Ridge System. *Andean Geology* 36(1): 3-16.

- 1048 Vila, T., Lindsay, N., Zamora, R. (1996) Geology of the Manto Verde copper deposit, northern Chile: A
 1049 specularite-rich, hydrothermal-tectonic breccia related to the Atacama fault zone. Society of
 1050 Economic Geology Special Publication 5: 157–170.
- 1051 Vivallo, W., Díaz, A., Jorquera, R. (2008) Yacimientos metalíferos de la región de Atacama, Escala
 1052 1:500.000. Carta Geológica de Chile, Serie Recursos Minerales y Energéticos (n.27).
 1053 SERNAGEOMIN, Santiago, 72 pp.
- 1054 Vivallo, W., Hemnriquez, F., Espinoza, S. (1995) Metasomatismo y alteración hidrotermal en el distrito
 1055 ferrífero Cerro Negro Norte, Copiapó, Chile. Revista Geológica de Chile 22: 75-88.
- 1056 Vivallo, W. (2009) Yacimientos de óxidos de Hierro-Cobre-Oro en Chile. XII Congreso Geológico
 1057 Chileno: s11_060.
- 1058 Wallace, R. (1951) Geometry of shearing stress and relation to faulting, Journal of Geology 59: 118-130.
- 1059 Whitney, D., Evans, B. (2010) Abbreviations for names of rock-forming minerals. American Mineralogist
 1060 95: 185-187.
- 1061 Woodcock, N.H., Mort, K. (2008) Classification of fault breccias and related fault rocks. Geological
 1062 Magazine 145(3): 435–440.
- 1063 Yamaji, A. (2000) The Multiple Inverse Method: A new technique to separate stresses from
 1064 heterogeneous fault-slip data. Journal of Structural Geology 22: 441-452.
- 1065 Žalohar, J., Vrabec, M. (2007) Paleostress analysis of heterogeneous fault-slip data: The Gauss method.
 1066 Journal of Structural Geology 29: 1798-1810.
- 1067 Žalohar, J., Vrabec, M. (2008) Combined kinematical and paleostress analysis of fault-slip data: The
 1068 multiple-slip method. Journal of Structural Geology.30: 1603-1613.

1069

1070 Figure Captions

1071

1072 Figure 1. General location of Fe-rich deposits in northern Chile showing the general trace of the AFS
 1073 (after Cembrano et al., 2005) and of the “Cretaceous Iron Belt” (e.g. Sillitoe, 2003).

1074 Figure 2. (a) Contour density (each 2%) plot of poles of all measured structural elements at Dominga and
 1075 indicating preferential orientations (A to E). Rose diagrams (petals each 5°) showing: (b) same
 1076 data as (a) as well as identified preferential strike directions; (c) the strike orientation of
 1077 structural elements with complete fault datum (fault-slip data); (d) the strike orientation of

1078 ultracataclasites and cataclasites with S-C textures. (e) Half-rose diagram (5° petals) showing
1079 the preferential strike direction of veins with different mineral fillings.

1080 Figure 3. Examples of the variety of structural elements outcropping at Dominga: (a) foliated, right-lateral
1081 ultracataclasite with S-C texture; (b) ultracataclasite with large Mag crystals; (c) contiguous set
1082 of structural elements (cataclasites, fault-breccias) forming the composite structural element of
1083 El Tofo Deformation Band; (d) hydrothermal breccia with Mag>Act(>>Ap?) matrix, including
1084 large Fe-altered clast of the Punta del Cobre Formation; (e) hydrothermal breccia with Mag-
1085 rich matrix and large clast of the Porphyric Dioritic Complex (andesite); (f) slickenlines on a
1086 slip-surface developed on the Porphyric Dioritic Complex; (g) slickenfibers of Hem (specular)
1087 on an air-exposed fault-vein; (h) quartz veins with two different textures showing cutting
1088 relationship; (i) subvertical, centimeter-wide, Mag-rich veins cutting the Punta del Cobre
1089 strata; (j) histogram of occurrence and (k) box-and-whisker plot of thicknesses of the different
1090 structural elements filtered by preferential striking direction.

1091 Figure 4. Examples of mapped key locations at the Dominga district. (a) Satellite view (Google Earth®)
1092 showing the Dominga district (datum UTM19S, WGS82). (b) to (e) insets show mapped
1093 lineaments and structural elements.

1094 Figure 5. Lower hemisphere, equal-area projections of density contours of P (left) and T (right) strain
1095 axes from (a) entire fault-slip data and from the filtered fault-slip data: (b) ESS, (c) S-C-
1096 derived fault-slip data, (d) ETSS, (e) ISS, and (f) LSS.

1097 Figure 6. Lower hemisphere, equal-area projections with solutions of principal stress axes estimated with
1098 the MIM from (a) the entire (unfiltered) fault-slip data, and (b) the S-C-derived (identified
1099 clusters are labeled A to F, as indicated on both the stereogram and the distribution of ϕ). (c)
1100 histogram of misfit angles between measured fault-slip data and estimated stress field
1101 (indicated). (d) sets of structural elements activated under each of the different estimated stress
1102 fields (A-F) showing their compatible displacement direction and the estimated direction of
1103 principal stress axes color coded according to its ϕ value.

1104 Figure 7. Relative chronology among and between key minerals observed at Dominga together with
1105 defined alteration/mineralization stages (I-IV) (width of triangles indicates relative abundance).
1106 (b) to (k) micro-photographs with examples of the occurrences and relationships of key

1107 minerals: (b) pervasive Mag-Bt alteration (stage I) of strata from Punta del Cobre Formation;
1108 (c) coarse-grained Mag-Act association (stage IIa); (d) Magnetite porphyroblast with Qtz
1109 syntectonic rims (stage IIa) in a fine-grained Mag-rich matrix (stage I); (e) matrix of
1110 hydrothermal breccia from the ESS with Mag-Act-Ap-Qtz (stage IIb) association; (f)
1111 occurrence of Ab-Ep-Qtz association (stage IIIa) in rocks of the Porphyric Dioritic Complex;
1112 (g) intergrowth of Aln and Ccp together with Anh (stage IIIb); (h) veins with infill of Qtz and
1113 Ep (stages III-IV) association; (i) anhedral Vrm crystals (stage IIIb) cut by vein of Cal (stage
1114 IV); (j) partial view of a Cal-rich vein with lattice and banded textures, together with tiny
1115 crystals of Ccp (stage IV); (k) partial view of a vein with Hem and Qtz association filling
1116 (stage IV). Microphoto (b) taken under transmitted polarized light and (j) under reflected
1117 polarized light, all others under transmitted cross-polarized light.

1118 Figure 8. Conceptual sketch profile view of a (strike-slip) structural element and its relation to different
1119 structural levels (after Sibson, 1987; Scholz, 2002; Holdsworth et al., 2011).

1120 Figure 9. Samples and data used for isotopic dating. (a) Photo (upper) and SEM image (lower) of mineral
1121 association seen on sample DS11-134 (see Table 1) used for Re-Os isotopic dating. (b) Same
1122 as (a) but showing sample DN11-136 used for U-Pb isotopic dating, (c) Concordia U-Pb plot
1123 with calculated age for the apatite (data-point error ellipses are 68.3%).

1124 Figure 10. General estimated directions of principal (a) strain and (b) stress axes for the entire fault-slip
1125 data (top) and for each of the identified structural systems (senses and amounts of rotation/shift
1126 of principal axes from one system to the other are indicated). (c) Relative time-trajectory of the
1127 estimated maximum principal strain and stress axes for each structural system. Sense and
1128 amount of rotation/shift plus the main tectonic setting, TP (transpressive) or TT (transtensive)
1129 are indicated.

1130 Figure 11. Compilation of geochronological ages of regional and local tectonic, magmatic, structural and
1131 of alteration/mineralization stages identified and defined at Dominga and at other Fe-rich
1132 deposits in the “Cretaceous Iron Belt”. TT: Transtensional, TP: Transpressional

1133 Figure 12. Schematic cartoon showing the tectono-metallogenic relation and evolution between and
1134 among the different structural systems and defined alteration/mineralization stages (I to IV).

1135

Figure 1
Click here to download Figure: Veloso et al. - Figure 1.tif

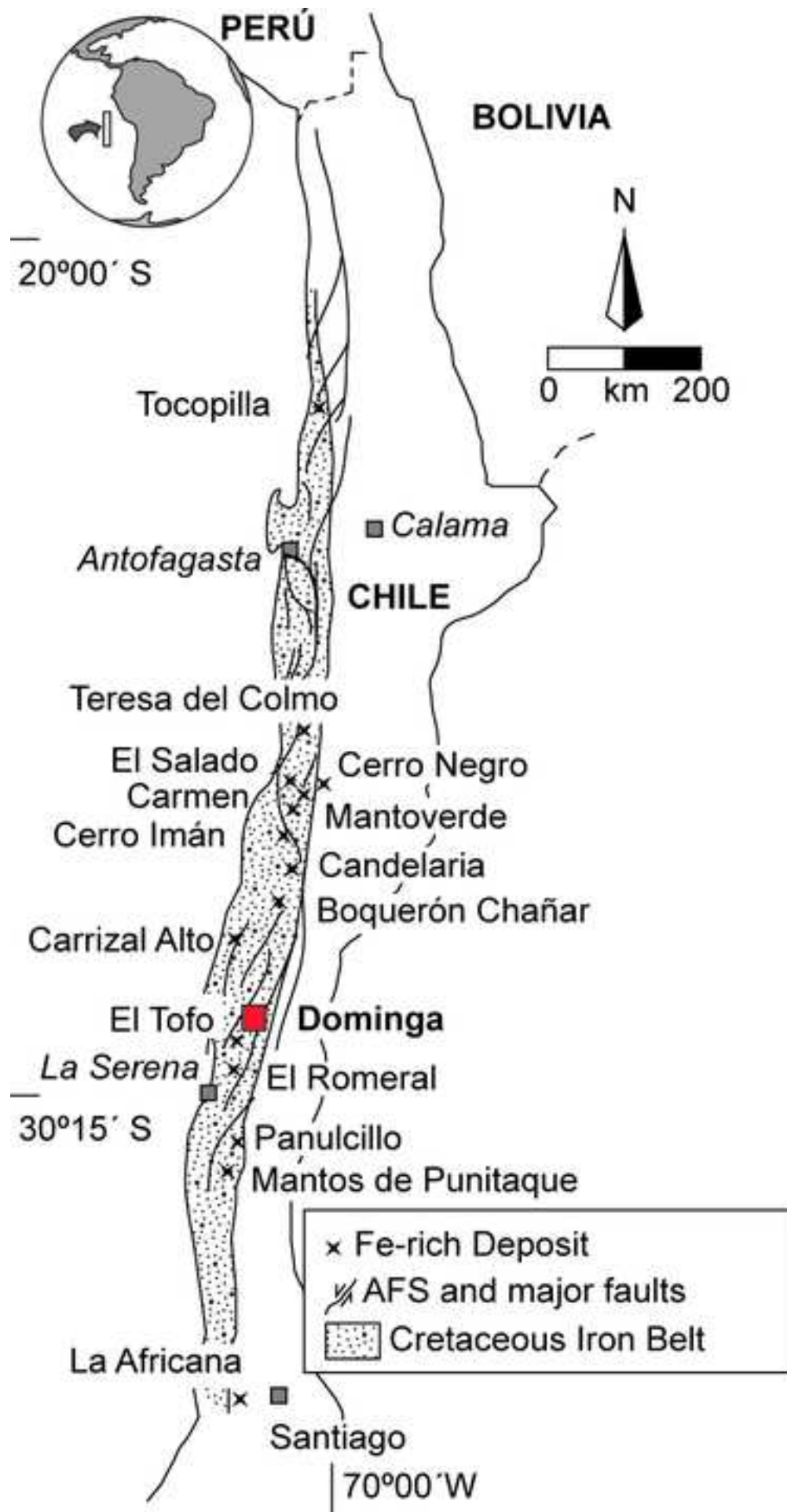


Figure 2

[Click here to download Figure: Veloso et al. - Figure 2.tif](#)

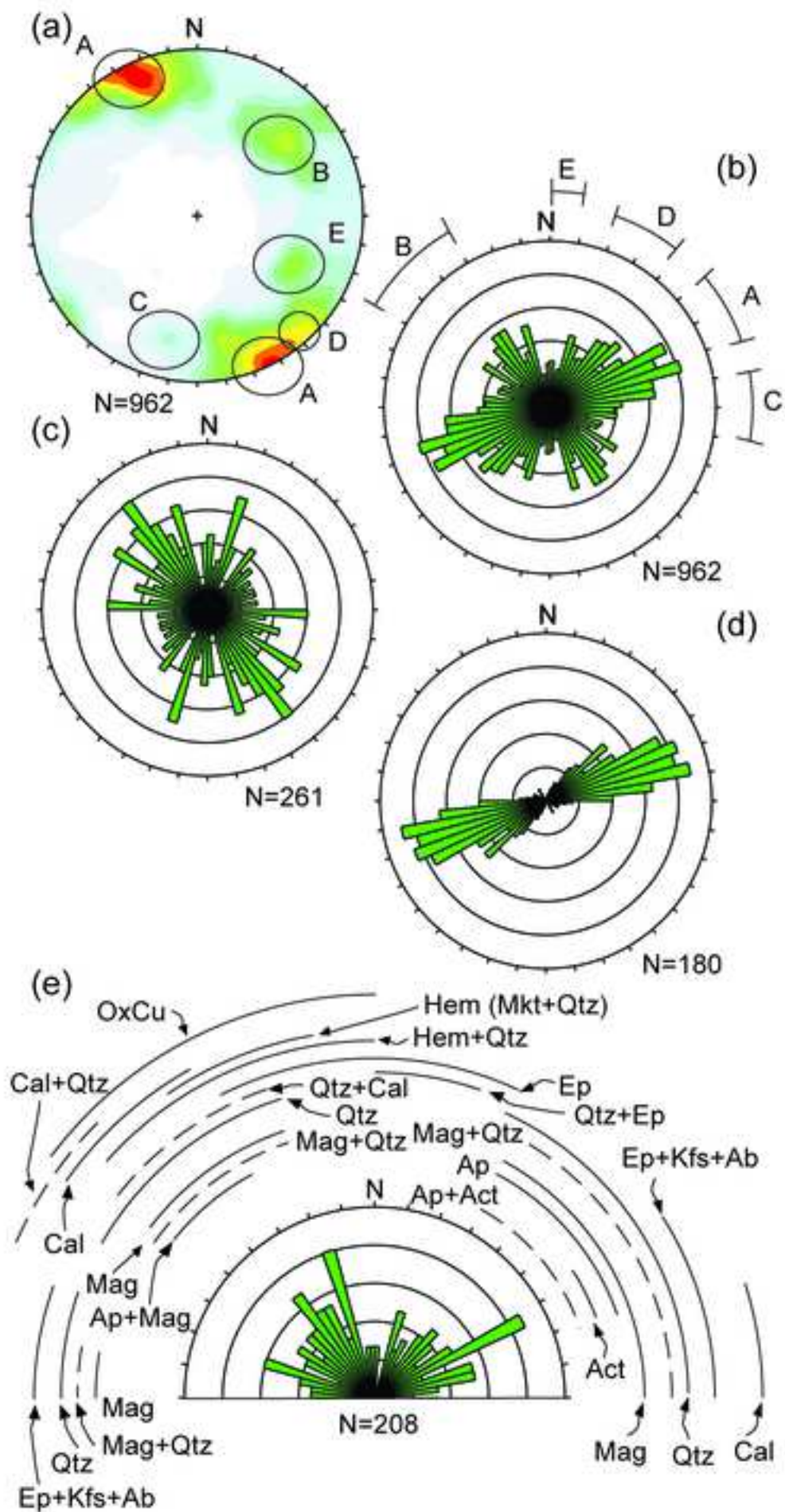


Figure 3

[Click here to download Figure: Veloso et al. - Figure 3.tif](#)

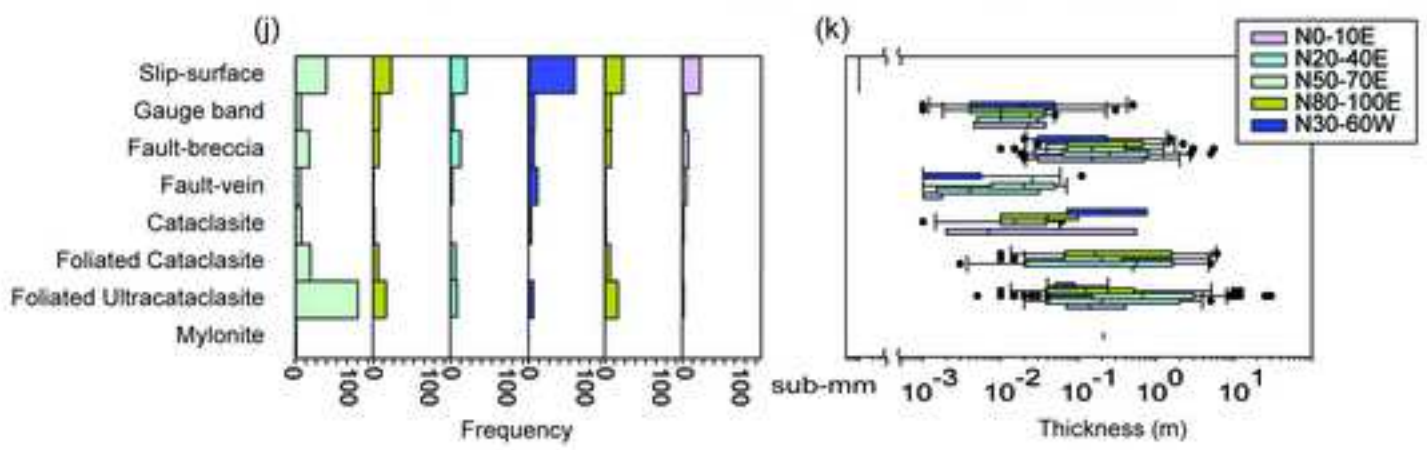
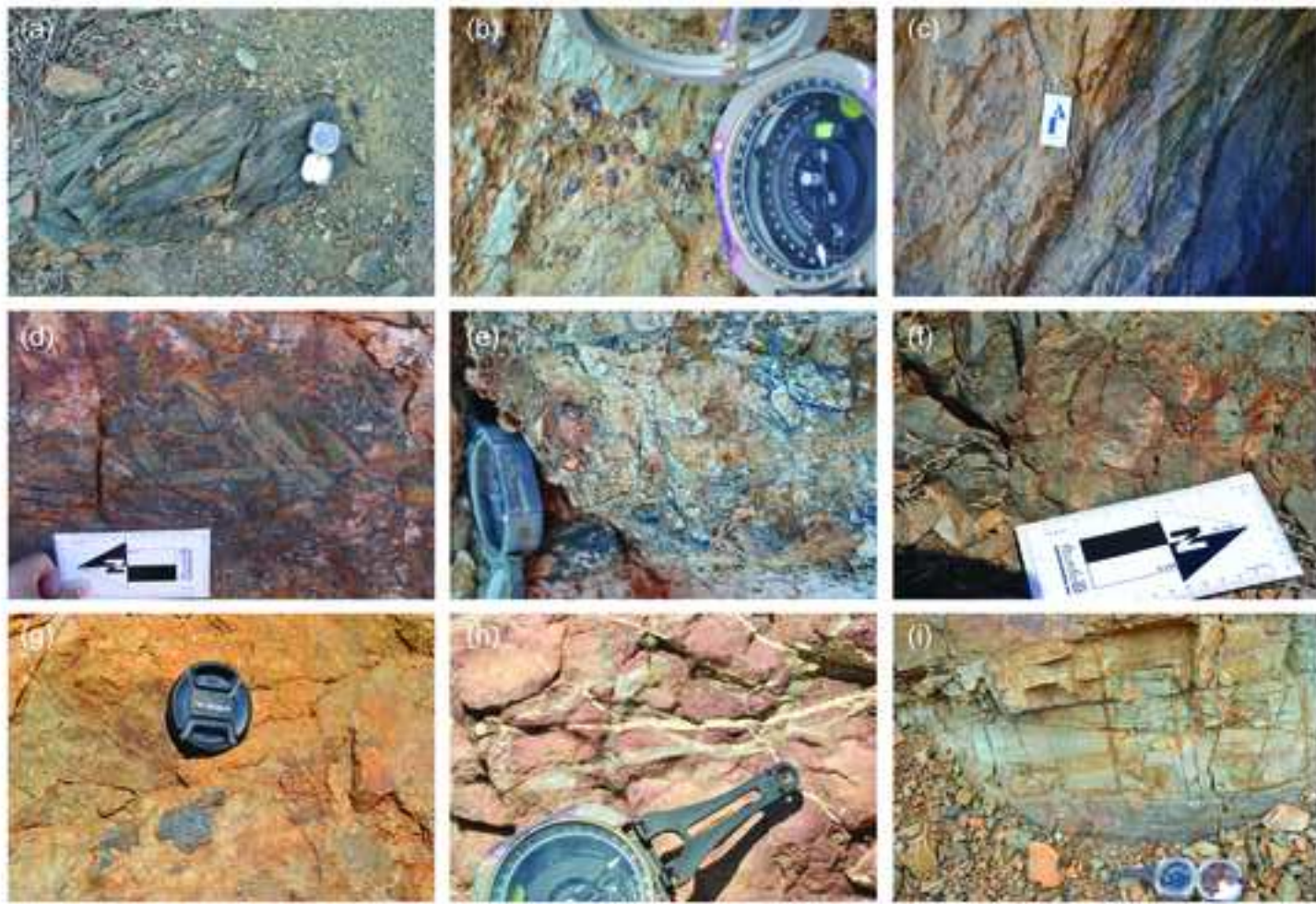


Figure 4
Click here to download Figure: Veloso et al. - Figure 4.tif

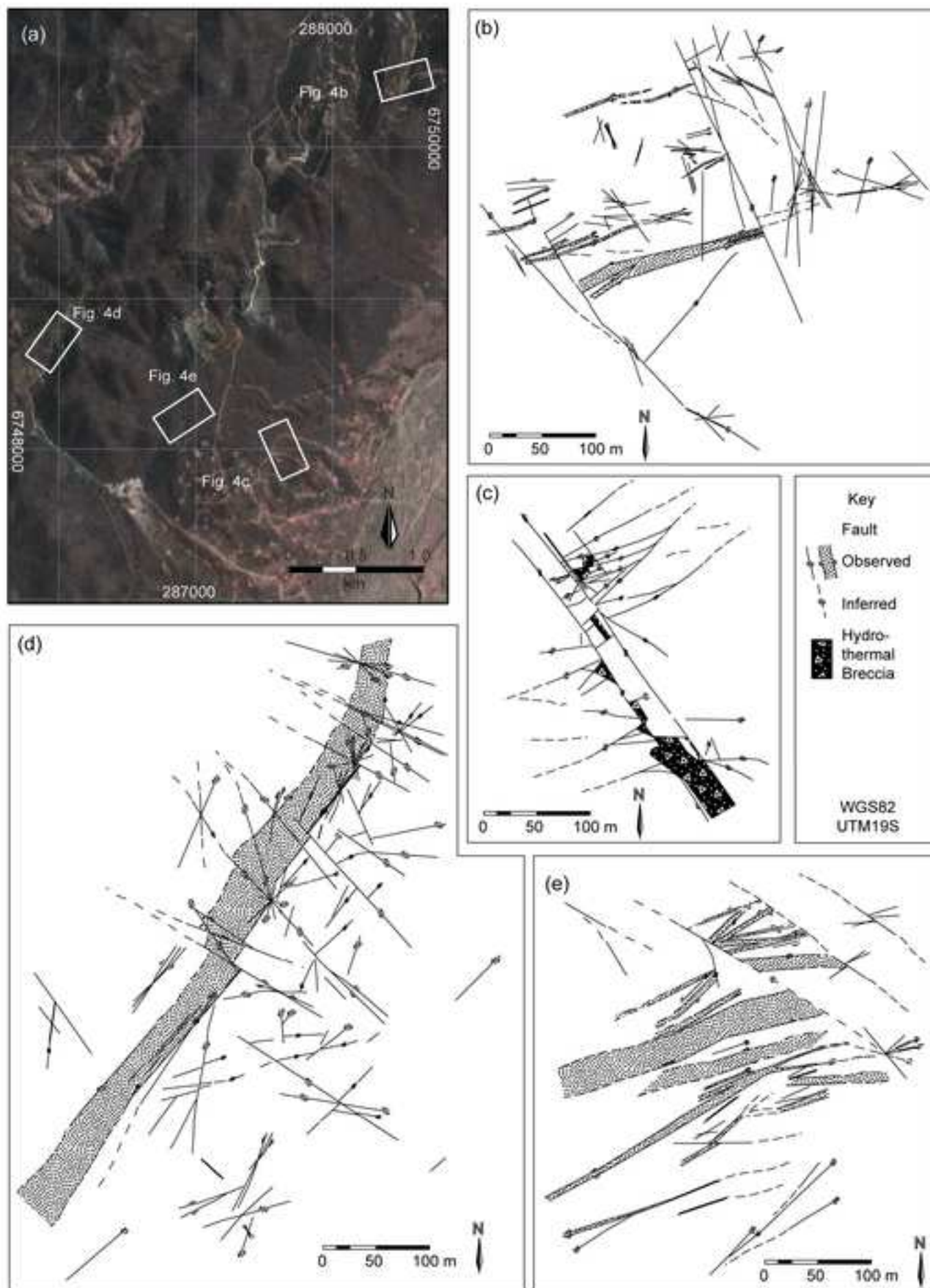


Figure 5

[Click here to download Figure: Veloso et al. - Figure 5.tif](#)

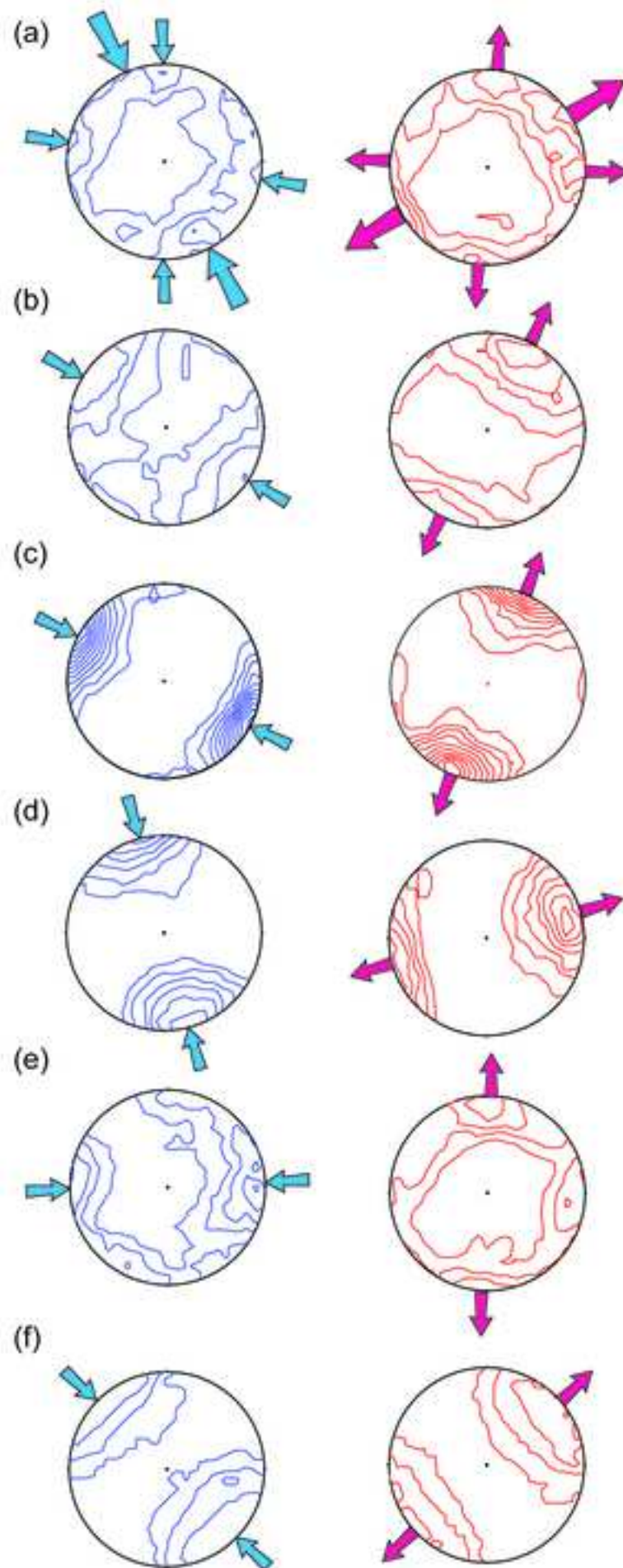


Figure 6
[Click here to download Figure: Veloso et al. - Figure 6.tif](#)

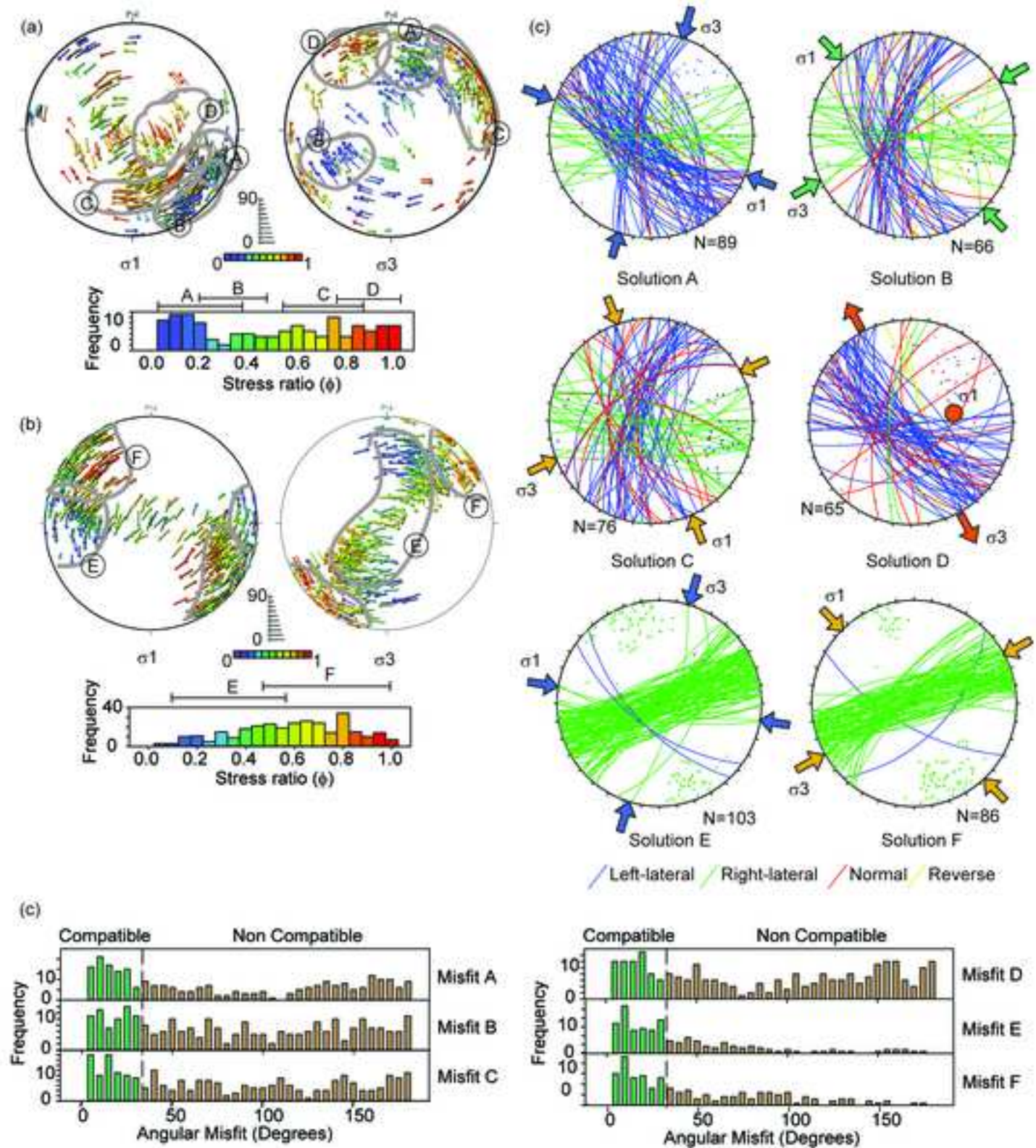


Figure 7
[Click here to download Figure: Veloso et al. - Figure 7.tif](#)

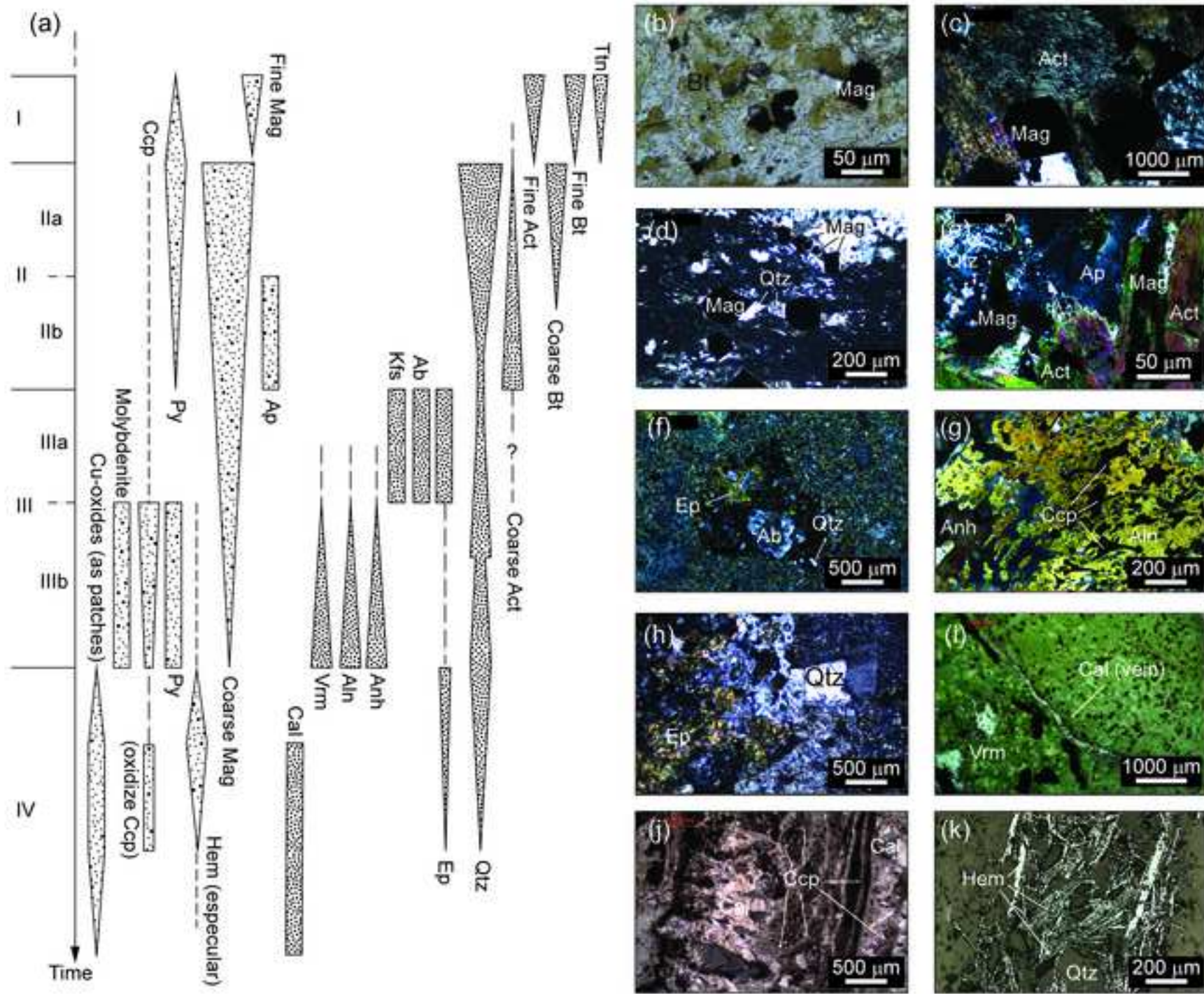


Figure 8
Click here to download Figure: Veloso et al. - Figure 8.tif

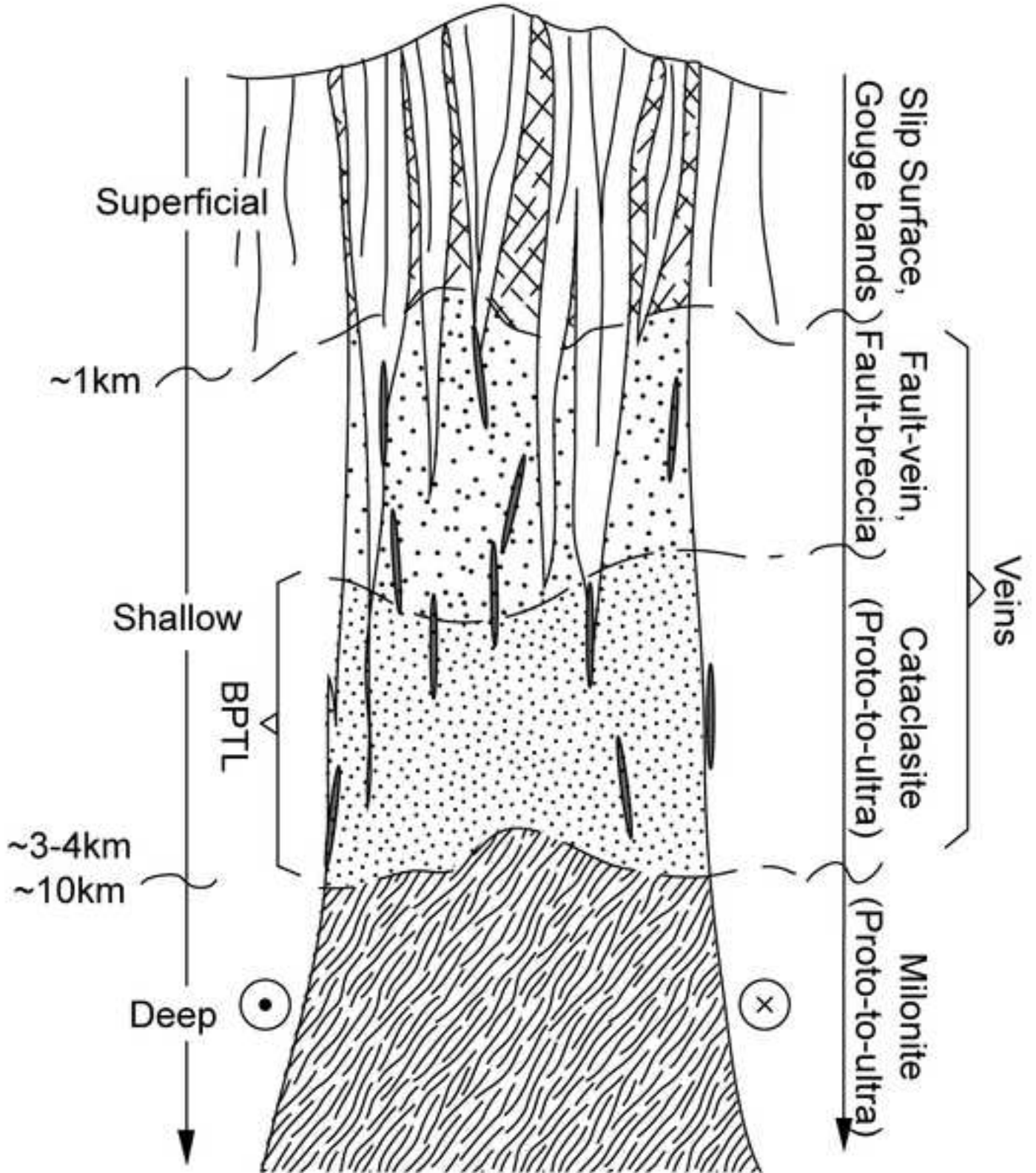


Figure 9

[Click here to download Figure: Veloso et al. - Figure 9.tif](#)

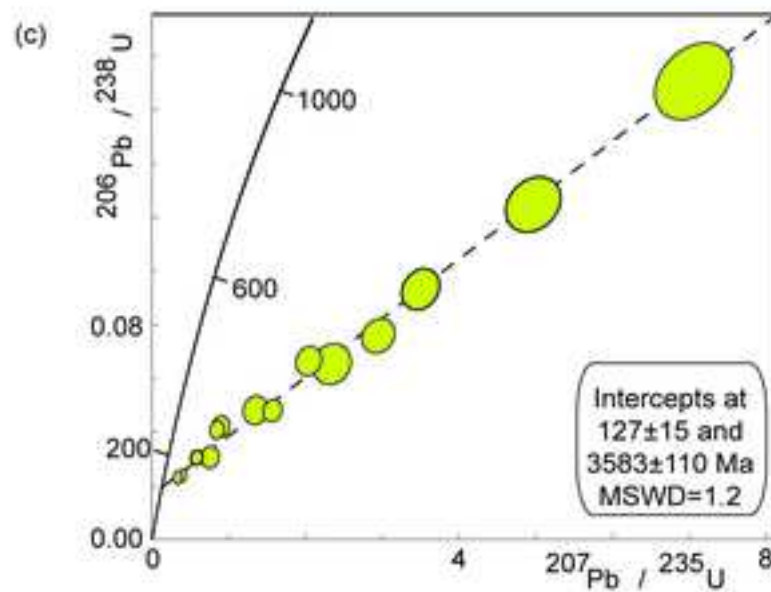
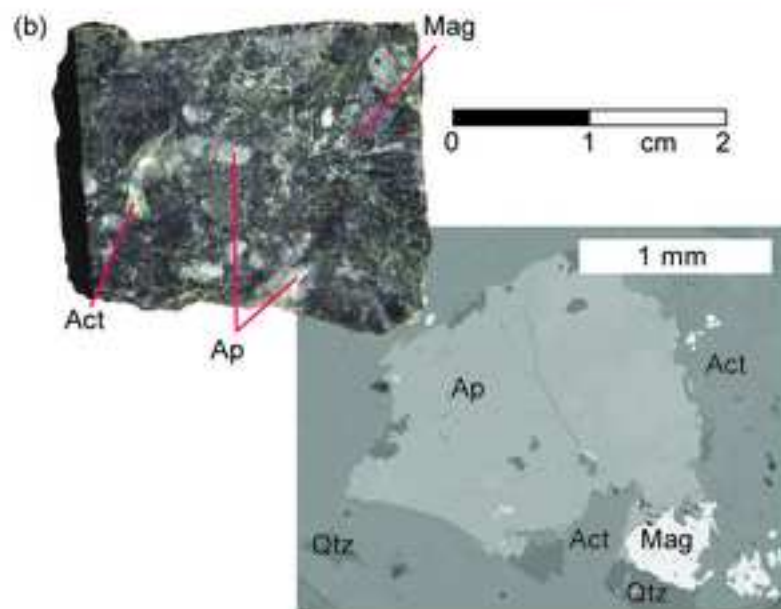
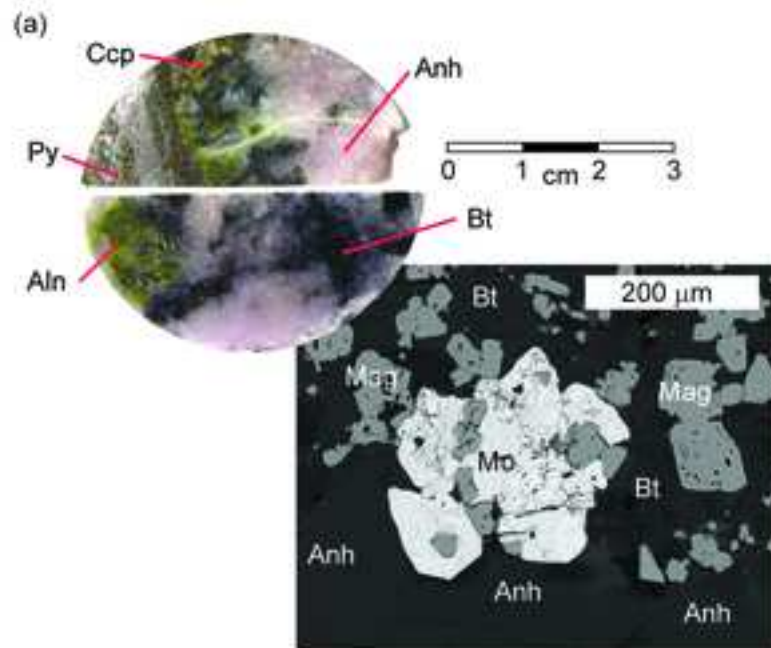


Figure 10
[Click here to download Figure: Veloso et al. - Figure 10.tif](#)

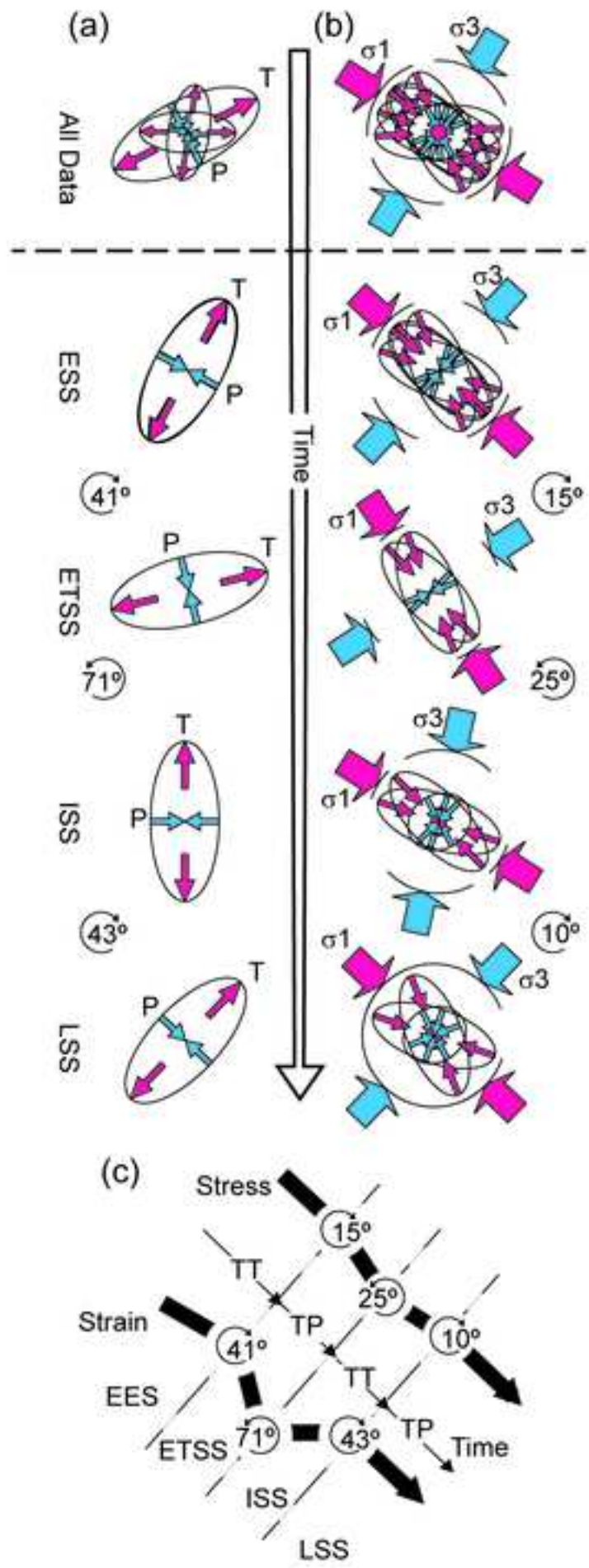


Figure 11
 Click here to download Figure: Veloso et al. - Figure 11.tif

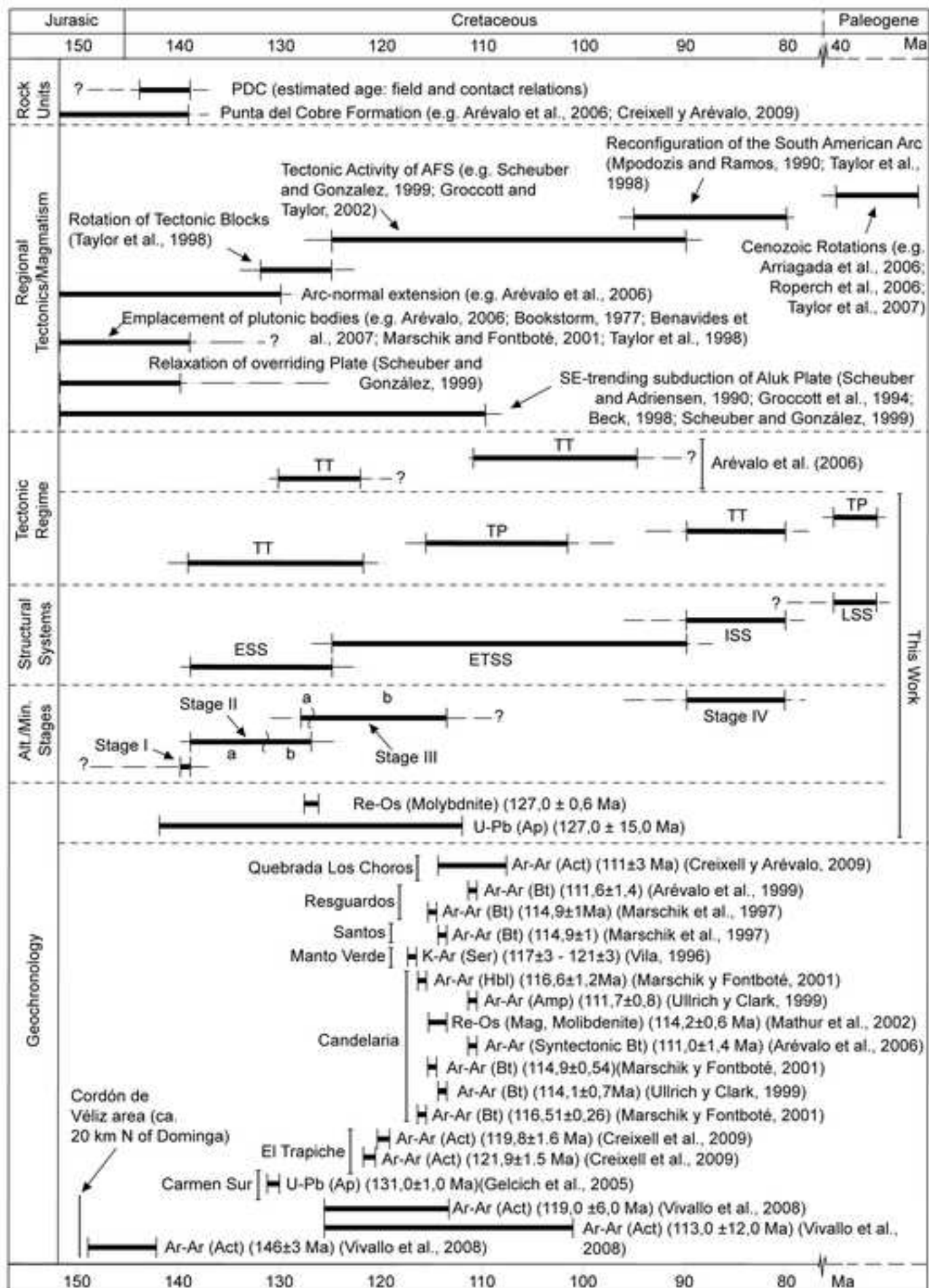
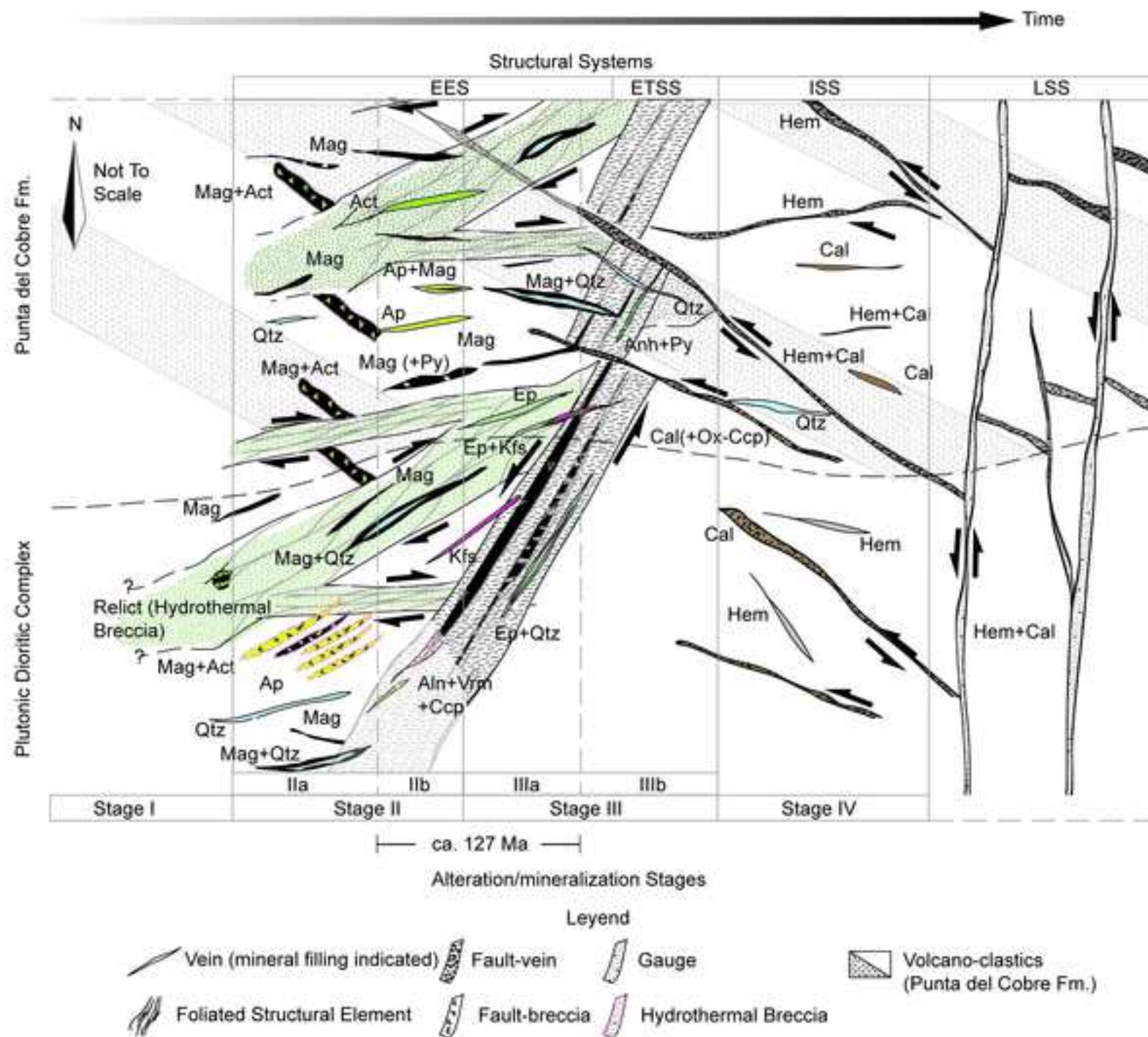


Figure 12

[Click here to download Figure: Veloso et al. - Figure 12.tif](#)



26

27 Table 1. Geochronologic isotopic data.

28

Re-Os data for molybdenite

Sample	Weight (mg)	Re (ppm)	$\pm 2\sigma$	^{187}Re (ppm)	$\pm 2\sigma$	^{187}Os (ppb)	$\pm 2\sigma$	Age (Ma)	$\pm 2\sigma$
DS11-134	0.005	886.46	8.03	557.16	5.05	1180.92	10.45	127.09	0.65

U/Pb data for apatite

Sample	Concentration (ppm)					Ratio			
	U	Th	Th/U	$^{207}\text{Pb}/^{206}\text{Pb}$	1σ	$^{207}\text{Pb}/^{235}\text{U}$	1σ	$^{206}\text{Pb}/^{238}\text{U}$	1σ
DG11-136-G1-01	0.28	1.39	5.06	0.260	0.026	2.344	0.164	0.065	0.005
DG11-136-G1-02	0.41	1.01	2.49	0.272	0.018	3.499	0.162	0.093	0.005
DG11-136-G1-03	0.51	1.10	2.14	0.222	0.016	2.043	0.110	0.67	0.004
DG11-136-G1-04	0.51	1.13	2.23	0.203	0.021	1.350	0.106	0.048	0.004
DG11-136-G1-05	.42	1.42	3.38	0.155	0.016	0.900	0.075	0.042	0.003
DG11-136-G2-01	1.29	0.38	0.30	0.121	0.013	0.400	0.036	0.024	0.002
DG11-136-G2-02	0.84	0.83	1.00	0.151	0.013	0.850	0.059	0.041	0.002

DG11-136-G2-03	0.54	0.97	1.78	0.179	0.024	0.758	0.077	0.031	0.003
DG11-136-G2-04	0.58	0.79	1.36	0.139	0.015	0.584	0.052	0.031	0.002
DG11-136-G2-05	1.18	0.57	0.48	0.106	0.013	0.339	0.036	0.023	0.002
DG11-136-G3-01	0.37	1.44	3.93	0.281	0.020	2.950	0.143	0.076	0.004
DG11-136-G3-03	0.25	1.15	4.62	0.288	0.020	4.966	0.236	0.125	0.007
DG11-136-G3-04	0.24	0.39	1.58	0.299	0.020	7.051	0.332	0.171	0.009
DG11-136-G3-05	1.19	16.02	13.42	0.237	0.018	1.572	0.081	0.048	0.003

29

30

